

Article

Geochemical Characteristics, Zircon U-Pb Ages and Lu-Hf Isotopes of Pan-African Pegmatites from the Larsemann Hills, Prydz Bay, East Antarctica and Their Tectonic Implications

Shi Zong ¹, Yingchun Cui ^{1,*}, Liudong Ren ², Hao Zhang ¹, Shaocong Chen ¹, Weixuan Wang ¹ and Shenggui Li ¹

¹ Polar Research Institute of China, Shanghai 200136, China; zongshi@pric.org.cn (S.Z.); zhanghao@pric.org.cn (H.Z.); chenshaocong@pric.org.cn (S.C.); wangweixuan@pric.org.cn (W.W.); lishenggui@pric.org.cn (S.L.)

² Institute of Geology, Chinese Academy of Geological Sciences, Beijing 100044, China; ldren@cags.ac.cn

* Correspondence: cuiyingchun@pric.org.cn

Abstract: Prydz Bay is an important part of the Pan-African high-grade tectonic mobile belt. The focus of this investigation, by applying zircon LA-ICP-MS U-Pb geochronology, zircon Lu-Hf isotope systematics, and whole-rock geochemistry, is on Pan-African pegmatites in the Larsemann Hills of Prydz Bay, East Antarctica, their association with country rocks, and the formation conditions. Based on the obtained results, it is concluded that the pegmatites exhibit elevated levels of silica and alkali and possess peraluminous features. These pegmatites originated during the late Neoproterozoic–Early Cambrian (Pan-African) event, specifically in the D₂–D₄ stages. The D₂ stage occurred between 546 and 562 Ma, followed by D₃-stage pegmatites around 534 Ma. The pegmatites from the D₂–D₃ stages are considered to originate from Paleoproterozoic crustal materials, while there are at least two phases of pegmatites in the D₄ stage (~517 Ma and ~521 Ma). The D₄₋₁ pegmatite (~521 Ma) suggested both Paleo–Mesoproterozoic crustal origin, perhaps connected to extension. The D₄₋₂ pegmatite (~517 Ma) originated from the crust layers. In the Larsemann Hills, Pan-African pegmatites formed in a recurring regime of tension. Therefore, the obtained data elucidate that a Pan-African stretching process might have occurred in Prydz Bay.

Keywords: Pan-Africa; East Antarctica; Prydz Bay; plate suture zone; pegmatite



Citation: Zong, S.; Cui, Y.; Ren, L.; Zhang, H.; Chen, S.; Wang, W.; Li, S. Geochemical Characteristics, Zircon U-Pb Ages and Lu-Hf Isotopes of Pan-African Pegmatites from the Larsemann Hills, Prydz Bay, East Antarctica and Their Tectonic Implications. *Minerals* **2024**, *14*, 55. <https://doi.org/10.3390/min14010055>

Academic Editors: Mohamed Zaki Khedr and Richard M. Palin

Received: 30 November 2023

Revised: 29 December 2023

Accepted: 29 December 2023

Published: 31 December 2023



Copyright: © 2023 by the authors. Licensee MDPI, Basel, Switzerland. This article is an open access article distributed under the terms and conditions of the Creative Commons Attribution (CC BY) license (<https://creativecommons.org/licenses/by/4.0/>).

1. Introduction

Prydz Bay in East Antarctica is renowned for its role in deciphering the Earth's tectonic evolution during the Precambrian. This region has experienced both the Grenvillian orogeny (~1000 Ma) tectono-thermal event and the Early Paleozoic Pan-African (~530 Ma) tectono-thermal event. There are varying opinions on the P-T trajectory of the metamorphic process, with some proposing that it comprises two distinct high-grade metamorphic events [1–9]. Two contradictory perspectives exist regarding the tectonic attributes of the two metamorphic events in the Prydz belt. The clockwise P-T trajectory of the tectonic belt suggests the occurrence of a Pan-African collisional orogenic process. The Prydz belt is directly linked to the ultimate convergence of the East Gondwana paleocontinent during the early Paleozoic [1,10–21]. The Prydz belt is a complex metamorphic belt that underwent several metamorphic stages, with the Grenville metamorphism being the most prominent. This metamorphism is linked to the collisional orogenic event that occurred during the formation of the Rodinia supercontinent. Similarly, Pan-African metamorphism is considered the result of the intracontinental adjustment effects of the East Gondwana collisional orogeny [6,22–34].

The Larsemann Hills experienced significant magmatic activity and intense crustal melting activity around 500 Ma, prompting a comprehensive investigation into their crustal evolution [35,36]. During Pan-African magmatic activity, a notable abundance of granitic

rocks formed, exhibiting high differentiation and originating from the crystallization of residual magmas with increased volatility [37–42]. It is essential to emphasize that pegmatites can achieve complete crystallization and differentiation only under specific conditions [42]. This holds particular significance during petrogenesis and mineralization, aiding in the identification of material sources and the understanding of geotectonic evolution [43].

The Larsemann Hills are defined by the presence of numerous coarse-grained, light-colored pegmatite veins. These pegmatites were formed at different stages during the Larsemann Hills' deformational history and are found either as flat bodies or as separate lenses that generally occupy structurally controlled positions, such as at fold hinges, in shear zones, and at boudin necks [2]. It is necessary to further strengthen the comprehensive correlation analysis among pegmatite veins, country rocks, and their tectonic context. Previous studies on the absolute age, and isotopic composition of Pan-African pegmatites are rare. This research focuses on Pan-African pegmatites in the Larsemann Hills, employing lithological and geochemical analyses. LA-(MC)-ICP-MS techniques are utilized for zircon dating, trace element analysis, and Lu-Hf isotope analysis. Through these studies, the pegmatite formation process can be effectively elucidated, shedding light on the nature of deep melting host rocks, clarifying the genesis of zircons in pegmatites, constraining the time of anatexis, and exploring the diagenetic relationship between the metamorphic evolution of Pan-African ultra-high-temperature rocks in the Larsemann Hills [7]. Additionally, examining the formation age and magmatic genesis of Pan-African pegmatites in the Larsemann Hills can provide a better understanding of the magmatic activity and structural features of Prydz Bay.

2. Geological Background

The Larsemann Hills, located in Prydz Bay, East Antarctica, constitute one of the three bedrock outcrops in the area (Figure 1). These hills are vital for the study of the late Precambrian high-grade metamorphic terrane of the region [44–46]. The terrain encompasses high amphibolite facies to granulite facies to psammitic and pelitic paragneiss, along with a small quantity of pyroxene-bearing mafic granulite and leucogranitic orthogneiss [6,41,46,47].

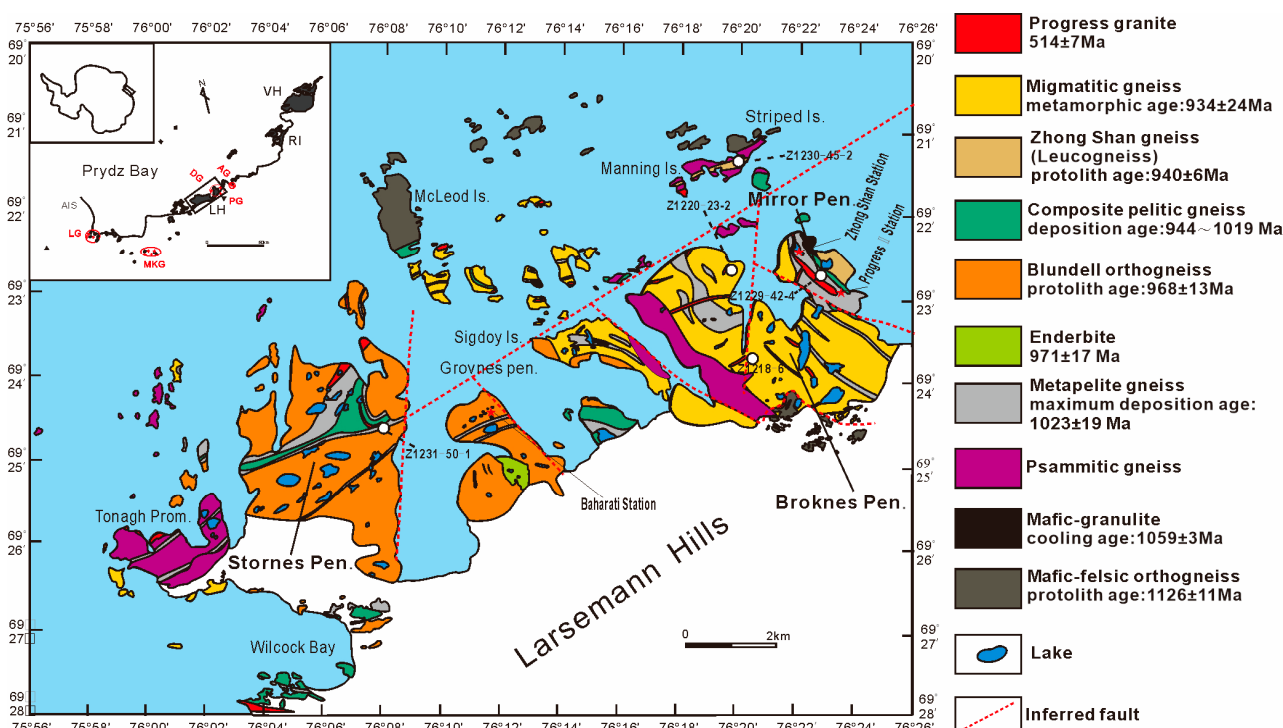


Figure 1. The geological map of the Larsemann Hills, Prydz Bay, East Antarctica, and the sample locations show major lithological units [6,24,28,33,48]. Insert shows the position of the Larsemann

Hills in Prydz Bay. Abbreviations: LH (Larsemann Hills), AIS (Amery Ice Shelf), VH (Vestfold Hills), RI (Rauer Islands), RG (Rauer Group), DG (Dalkoy granite), MKG (Munro Kerr granite), PG (Progress granite), LG (Landing granite), AG (Amanda granite).

The Brattstrand paragneiss stands as the primary rock formation, comprising various metasedimentary units. Within these units, certain types are recognized for their high levels of boron (B), exemplified by tourmaline quartzite and a suite of borosilicate minerals like grandidierite, kornerupine, and tourmaline [3,49,50]. This paragneiss exhibits significant features of partial melting, resulting in the formation of diverse gneiss and migmatites that feature mixtures of sillimanite and cordierite [2,5,18,24,36,51]. The Søstrene orthogneiss, primarily composed of a mafic–felsic magmatic complex, is typically preserved in pelitic granulite in lens-, lentil-, and sausage-shaped forms. Following its peak in metamorphism, an actual occurrence of deep melting took place, leading to the formation of multiple pegmatites, migmatites, and garnet-containing granites. These occurrences were distributed among syenite granites and monzonitic granites [6,24,52] (Figure 1). The granite is syn- and post-tectonic, and the elongated rock aligns with the overall distribution of gneiss in the surrounding rock where it is emplaced [12,53].

The distribution of the different rock types has a NE–SE direction. Most of the sequence is represented by metamorphic lithotypes. The primary tectonic line in the Larsemann Hills follows a NEE–SWW direction, while the eastern Mirror peninsula aligns NNW–SSE, forming a complex compound syncline that wraps in a NEE direction [54]. Wang’s [55] research categorizes the deformation in the Larsemann Hills into four phases. The first phase of regional deformation (D_1) occurred during the Grenvillian orogeny associated with the peak metamorphic event (M_1). The second phase of deformation (D_2) resulted in tightly closed asymmetric folds. The third phase of deformation (D_3) exhibited significant tensor ruptures that cut through the asymmetric folds formed in D_2 . Subsequently, magma intruded along tensional fracture surfaces, creating granite veins. Finally, in the D_4 stage, a set of nearly equidistant and densely arranged upright broken cleavages developed (Table 1).

Table 1. Main geological events in the Larsemann Hills and adjacent areas of East Antarctica (after Wang, 2002 [55]).

	D_4 : Further stretching on the basis of D_3 (development of nearly equidistant dense upright cleavages)
Pan-African period	D_3 : N–S stretching event
	D_2 : WNW thrust event M_2 : Granulite facies’ metamorphism
	D_{1-2} : Act II of slow return stage
	Syntectonic perilla granite intrusion
Grenville period	D_{1-1} : (S_1 foliation of Bt–Sil–Qtz in Grt) M_1 : Granulite facies’ metamorphism
	Metasedimentary rocks
	Mafic–felsic composite gneiss

3. Analytical Methods

3.1. Major and Trace Elements

The samples were subjected to dissolution in a mixture of HNO_3 and HF. Major element analyses were performed using X-ray fluorescence (XRF), while the analysis of trace elements was performed utilizing a Perkin-Elmer Sciex Elan 6000 ICP-MS instrument [56]. All experiments were carried out at the laboratory of Hebei Regional Geology and Mineral Resources Survey and Research Institute, China (Langfang, China).

3.2. Zircon U-Pb Dating

The samples were crushed by conventional methods, and zircons were subsequently separated using a conventional flotation method. Zircon particles with bipyramidal-prismatic and transparent properties were handpicked under a binocular lens for further analysis. The chosen zircon grains were affixed to double-sided adhesive and, after undergoing the epoxy resin fixation, curing, and surface polishing process, were subjected to zircon micrography and cathodoluminescence photography. Cathodoluminescence (CL) imaging on the zircon grains was performed using a JEOL scanning electron microscope (SEM) equipped with a Gatan CL detector (Oxford, UK) at Nanjing Hongchuang Geological Exploration Technology Service Co., Ltd. in China (Nanjing, China). U-Pb zircon geochronology was carried out using laser ablation inductively coupled plasma mass spectrometry (LA-ICP-MS) at Beijing Createch Test Technology Co., Ltd. in China (Beijing, China). Laser sampling utilized an ESINWR 193 nm laser ablation system, and ion signal intensity was determined using an Analytik Jena PQMS Elite ICP-MS instrument, 91500, and GJ-1 was used as the standard materials for calibration, with operating conditions consistent with Zong et al. [9]. All errors were reported within 1 standard deviation (σ). Offline raw data selection and integration of background and analyte signals, as well as time drift correction and quantitative calibration for U-Pb dating, were performed using ICPMSDataCal (V10.0) [57]. Age calculations and concordance plots were generated using Isoplot /Ex_ver3 [58].

3.3. Zircon Lu-Hf Isotope Analysis

Laser ablation multi-collector inductively coupled plasma mass spectrometry (LA-MC-ICPMS) was employed for the *in situ* analysis of zircon Hf isotopes at the State Key Laboratory of Geological Processes and Mineral Resources, China University of Geosciences (Wuhan). The analyses were carried out using Neptune Plus MC-ICP-MS in combination with a GeoLas 2005 ArF-excimer laser ablation system (German Thermo Fisher Science, Dreieich, Germany).

4. Petrography and Mineralogy

Five samples were collected from various locations (Figure 1), including granitic pegmatite (Z1220-23-2) and plagioclase pegmatite (Z1218-6) from Broknes Peninsula, syenite pegmatite (Z1229-42-4) from Mirror Peninsula, plagioclase pegmatite (Z1230-45-2) from Manning Island, and granitic pegmatite (Z1231-50-1) from Stornes Peninsula.

The granitic pegmatite (Z1220-23-2) outcrop, with a gray-white appearance, spans tens of centimeters, displaying a penetrating invasion (Figure 2a). The primary rock-forming minerals include quartz (30%–35%), K-feldspar (20%–25%), plagioclase (20%–25%), biotite (~10%), and magnetite (~5%). K-feldspar displays a self-shaped and semi-self-shaped plate-column structure (Figure 2b), with Carlsbad twinning. In contrast, plagioclase exhibits a plate-columnar shape and polysynthetic twinning. The quartz structure is irregularly granular with wavy extinction. Biotite is distributed within the pores of other minerals, exhibiting a relatively high degree of self-shaping. The plagioclase pegmatite (Z1218-6) outcrop is a few tens of centimeters wide, is light yellow, and forms a vein of penetrating intrusion (Figure 2c), surrounded by semi-pelitic gneiss. The primary rock-forming minerals are plagioclase (70%–75%), quartz (20%–25%), microcline (5%–10%), garnet (~5%), and biotite (~2%). Feldspar and garnet appear as large crystals, typically exceeding 5 mm. Plagioclase shows obvious polysynthetic twinning, while microcline exhibits apparent tartan twinning. Additionally, small black mica particles are distributed in the interstices of other minerals as sheets (Figure 2d).

The syenite pegmatite (Z1229-42-4) is exposed over a width ranging from tens of centimeters to several meters. It exhibits a flesh-red color and forms a vein throughout the intrusion. The surrounding rock consists of pelitic gneiss (Figure 2e), characterized by coarse-grained minerals with varying granulometry mostly exceeding 3 mm, displaying a medium-coarse-grained texture and massive structure. The primary rock-forming minerals include K-feldspar (70%–75%), quartz (20%–25%), garnet (~10%), biotite (~5%), and

sillimanite (~2%). K-feldspar is euhedral and semi-euhedral plate-columnar, with Carlsbad twinning. Notably, and a substantial number of fibrous sillimanite crystals develop in the contact zone between K-feldspar and garnet (Figure 2f).

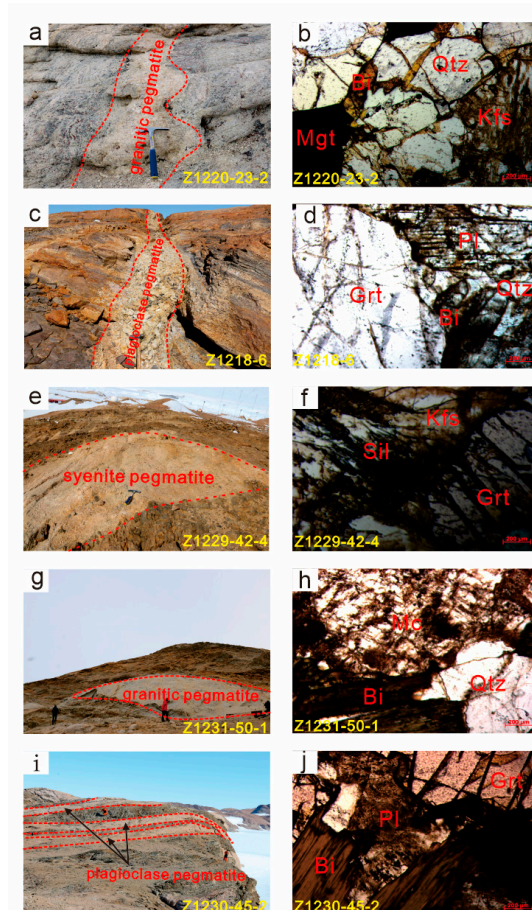


Figure 2. Field photographs (a,c,e,g,i) show the relationships between pegmatite and their surrounding rocks; microphotographs (b,d,f,h,j) show the contact relationship between rock-forming minerals. The mineral abbreviations is: Qtz (quartz), Bi (biotite), Kfs (K-feldspar), Pl (plagioclase), Grt (garnet), Mgt (magnetite), Mc (microcline).

The granitic pegmatite (Z1231-50-1) is exposed over a width of approximately 4 m, appearing grayish-white and predominantly lenticular in shape. It intrudes along the loose parts between pelitic gneiss layers (Figure 2g). Most minerals exhibit a highly crystalline structure, with uneven sizes, typically larger than 3 mm. Plagioclases display a medium-grained texture and an overall massive structure. The principal rock-forming minerals include microcline (60%–65%), quartz (20%–25%), plagioclase (20%–25%), biotite (~5%), and magnetite (~2%). Tartan twinning is observed in microcline, and plagioclase with polysynthetic twinning is abundant. Quartz occurs as irregular grains with obvious wavy extinction (Figure 2h).

The exposed width of the plagioclase pegmatite (Z1230-45-2) spans tens of meters, and the rock sample from the outcrop appears reddish due to weathering. Plagioclases, affected by weathering, take on a reddish color, which can be mistaken for K-feldspar in the field. These plagioclases are layered and intrude along the softer portions of the interlayer (Figure 2i), with psammitic gneiss as the enclosing rock. The minerals display a large geometric form, a uniform grain size, mostly 5 mm, and massive structures. The primary rock-forming minerals are plagioclase (60%–65%), microcline (20%–25%), quartz (15%–20%), biotite (~5%), garnet (~5%), and magnetite (~2%). The most representative mineral plagioclase is lamellar and columnar with a polysynthetic twin (Figure 2j).

5. Results

5.1. Major and Trace Elements

The samples Z1229-42-4 and Z1230-45-2 plot the intersection between the Shoshonite and high K (calc-alkaline) series' fields (Table 2; Figure 3a). The remaining samples (Z1220-23-2, Z1218-6, and Z1231-50-1) fall into the Shoshonite series field. The aluminum saturation index (A/CNK) for all the samples falls within the range of the aluminum saturation series (Figure 3b). The results from the standard mineral calculations indicate the presence of standard corundum molecules (Table 2), classifying all pegmatites as peraluminous magmatic rocks.

Table 2. Whole-rock major elements.

Sample	Z1220-23-2	Z1229-42-4	Z1231-50-1	Z1230-45-2	Z1218-6
SiO ₂	56.33	74.70	70.96	72.14	64.46
Al ₂ O ₃	22.38	12.59	16.00	15.40	19.06
TiO ₂	0.18	0.02	0.16	0.17	0.10
Fe ₂ O ₃	4.56	0.42	0.33	0.19	0.06
FeO	9.42	3.70	0.34	0.78	0.27
CaO	0.24	0.53	1.03	1.38	0.62
MgO	0.66	0.42	0.41	0.38	0.14
K ₂ O	4.17	5.27	6.53	5.56	12.01
Na ₂ O	0.73	1.28	3.36	3.17	2.61
MnO	0.05	0.37	0.00	0.01	0.00
P ₂ O ₅	0.14	0.07	0.12	0.06	0.09
LOI	0.51	0.52	0.53	0.56	0.31
Total	99.64	99.92	99.92	99.89	99.78
A/NK	3.91	1.61	1.27	1.37	1.10
A/CNK	3.85	1.47	1.13	1.13	1.05
Na ₂ O + K ₂ O	4.90	6.55	9.89	8.73	14.62
K ₂ O/Na ₂ O	5.70	4.13	1.94	1.75	4.60
Quartz	29.27	42.60	24.08	28.79	1.92
Anorthite	0.26	2.15	4.35	6.53	2.49
Albite	6.26	10.87	28.69	27.06	22.22
K-feldspar	24.94	31.34	38.85	33.09	71.37
Corundum	16.75	4.02	1.83	1.79	0.86
Hypersthene	15.13	8.19	1.13	1.98	0.64
Ilmenite	0.35	0.04	0.31	0.33	0.20
Magnetite	6.69	0.61	0.48	0.28	0.08
Apatite	0.33	0.17	0.28	0.14	0.22
Li	28.10	10.82	11.23	22.03	9.60
Be	4.41	0.56	0.43	1.06	0.45
Sc	1.17	7.09	4.22	1.50	1.22
V	27.65	2.19	15.27	13.27	8.00
Cr	4.01	6.80	6.61	6.24	4.33
Co	34.30	5.14	2.66	2.56	0.86
Ni	30.12	5.45	5.38	3.42	1.57
Cu	6.07	4.20	9.68	3.83	7.41
Zn	14.63	8.60	8.16	17.63	11.75
Ga	15.92	14.39	15.65	16.16	17.51
Rb	308.55	225.78	249.80	229.91	429.46
Sr	20.30	78.86	118.08	142.36	202.40
Y	1.91	21.72	18.73	2.78	1.65
Zr	88.52	84.28	33.73	17.04	20.68
Nb	6.61	2.01	2.96	4.67	2.76
Mo	1.81	0.21	0.39	0.01	0.49
La	21.80	177.72	75.21	18.29	13.64
Ce	46.49	36.50	28.76	27.77	19.90
Pr	5.37	29.73	16.19	2.69	1.87

Table 2. Cont.

Sample	Z1220-23-2	Z1229-42-4	Z1231-50-1	Z1230-45-2	Z1218-6
Nd	17.63	98.04	58.42	7.84	6.10
Sm	3.39	21.65	12.45	1.09	1.07
Eu	0.29	1.41	1.58	1.36	2.30
Gd	2.33	18.29	9.35	1.03	0.97
Tb	0.26	2.85	1.10	0.13	0.10
Dy	0.86	20.62	4.76	0.62	0.41
Ho	0.11	4.99	0.75	0.10	0.06
Er	0.32	15.72	1.85	0.22	0.17
Tm	0.05	2.83	0.23	0.03	0.03
Yb	0.31	16.97	1.19	0.13	0.16
Lu	0.05	2.01	0.14	0.02	0.02
Hf	3.10	3.62	1.18	0.54	0.55
Ta	0.45	0.11	0.16	0.20	0.13
Pb	55.74	45.65	22.26	42.16	65.22
Th	19.62	117.52	58.52	2.87	5.52
U	2.46	14.85	2.07	0.61	0.61
Σ REE	99.25	739.34	342.21	61.32	46.80
LREE/HREE	22.21	7.77	16.68	25.91	23.40
La_N/Yb_N	51.22	7.51	45.51	99.38	60.95
δEu	0.31	0.22	0.45	3.94	6.90

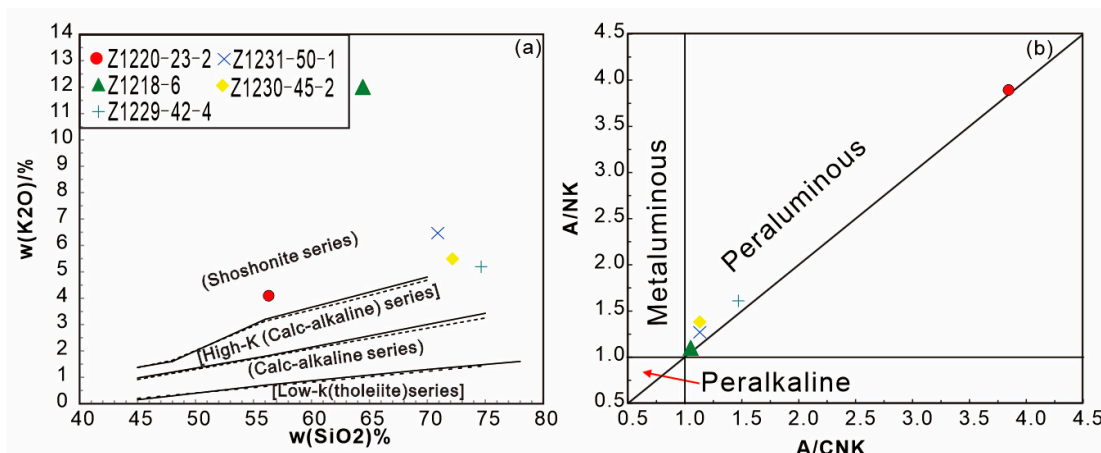


Figure 3. $\text{K}_2\text{O}-\text{SiO}_2$ ((a) solid line after Peccerillo and Taylor, 1976 [59]; dashed line after Middlemost, 1985 [60]) and $\text{A}/\text{CNK}-\text{A}/\text{NK}$ ((b), $\text{A}/\text{NK} = \text{Al}_2\text{O}_3/(\text{Na}_2\text{O} + \text{K}_2\text{O})$, $\text{A}/\text{CNK} = \text{Al}_2\text{O}_3/(\text{CaO} + \text{Na}_2\text{O} + \text{K}_2\text{O})$ after Maniar and Piccoli, 1989 [61]) plots for pegmatites from Larsemann Hills.

The samples show a strong differentiation in the distribution of rare-earth elements (REEs), with clear differentiation between light and heavy REEs' separation (Figure 4a). The plagioclase pegmatites, specifically Z1218-6 and Z1230-45-2, exhibit less-enriched light rare-earth elements (LREEs), with a notable positive Eu anomaly. The normalized values for the Eu anomaly are 3.94 and 6.90, respectively, determined by using the ratio of $2\text{Eu}_N/(\text{Sm}_N + \text{Gd}_N)$ [62] (Figure 4a). In the case of samples Z1220-23-2, Z1229-42-4, and Z1231-50-1, the chondrite-normalized REE patterns highlight a negative Eu anomaly. This suggests that the granitic melt underwent crystallization and separation, resulting in a highly evolved magmatic system. In the primitive mantle-normalized trace element plot, the high-field-strength elements (HFSE) such as Ba, Nb, Sr, P, and Ti are depleted, while elements like Rb, K, Th, and U, known as large-ion lithophile elements (LILE), appear to be more abundant (Figure 4b). This implies that the source material could be from ancient island arc material [62].

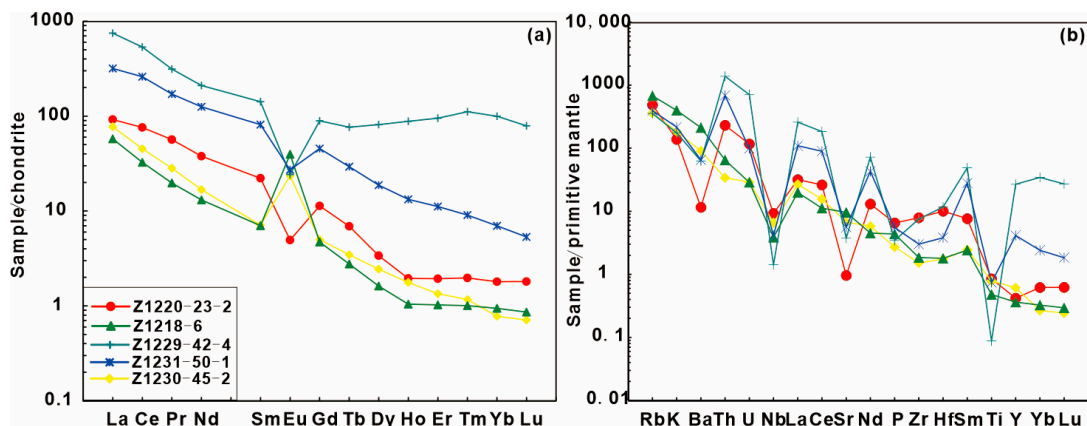


Figure 4. Chondrite-normalized REE patterns ((a) normalization values after Sun and McDonough, 1989 [63]) and primitive mantle normalized trace element patterns ((b), normalization values after McDonough and Sun, 1995 [64]) for pegmatites from Larsemann Hills.

5.2. *U-Pb Geochronology and Hf Isotope Systematics*

5.2.1. Zircon U-Pb Ages

The zircons from the granitic pegmatite (Z1220-23-2) have well-defined shapes, appearing as either short or long columns with a length of approximately 50 μm along the length/width ratio, ranging from 1:1 to 3:1. Cathodoluminescence (CL) examination reveals internal oscillatory zoning in magmatic zircons, and some zircons contain slight core inclusions (e.g., 28 and 35) (Figure 5a). CL images do not show evidence of fluid action in the process and later stage of zircon crystallization [65]. Thirty U-Pb dating analyses were conducted on the zircon grains, including 11 white zircons with ages ranging from 615 to 1116 Ma, showing dispersed ages of $^{206}\text{Pb}/^{238}\text{U}$. These zircons are considered inherited grains derived from the surrounding rocks during pegmatite crystallization. The inherited zircons experienced Pb losses after the Pan-African tectono-thermal events, resulting in their distribution in beads on the concordia diagram [6,24,33,66]. The newly formed magma zircons exhibit a distinct light gray color and show prominent growth zoning, with the weighted average age of $^{206}\text{Pb}/^{238}\text{U}$ at 517 ± 4 Ma (MSWD = 0.057, $n = 9$) (Figure 6a, Table 3).

The zircons found in the plagioclase pegmatite (Z1218-6) exhibit predominantly round or columnar shapes, with a length ranging from about 80 to 150 μm along the length/width ratio of 1:1–2:1. Cathodoluminescence (CL) images reveal a lack of developed zircon growth zones (Figure 5b). The color of the zircons is grayish black, and some zircons exhibit tiny cores. A total of 68 analyses were performed on the zircon grains. Among them, 24 zircons are distributed in a string of beads (Figure 6c), with individual $^{206}\text{Pb}/^{238}\text{U}$ ages ranging from 524 to 850 Ma. In CL imaging, these zircons generally appear dark, and the banding is not apparent, indicating that they are inherited grains derived from the surrounding rocks during pegmatite crystallization, while Pb loss is explained to a certain extent by the influence of the Pan-African events. According to the concordia diagram for $^{206}\text{Pb}/^{238}\text{U}$ and $^{207}\text{Pb}/^{235}\text{U}$, the weighted average age of $^{206}\text{Pb}/^{238}\text{U}$ is determined to be 521 ± 4 Ma (MSWD = 1.4, $n = 25$) (Figure 6c,d, Table 3).

The zircons in the syenite pegmatite (Z1229-42-4) exhibit irregular and incomplete shapes, with diameters ranging from approximately 50 to 150 μm . Cathodoluminescence (CL) images reveal the development of oscillatory zoning in zircon particles (Figure 5c). Most zircons display darker cores and lighter edges. A total of 35 analyses were conducted on zircon grains, and 16 zircon ages exhibit a bead-like distribution (Figure 6e), with $^{206}\text{Pb}/^{238}\text{U}$ ages ranging from 535 to 988 Ma. The darker cores and the lack of apparent banding in CL imaging suggest the inherited nature of these grains was derived from the surrounding rocks during crystallization, with some Pb loss due to the influence of the Pan-African events. For the $^{206}\text{Pb}/^{238}\text{U}$ and $^{207}\text{Pb}/^{235}\text{U}$ ages' concordia diagram, the

weighted average age of $^{206}\text{Pb}/^{238}\text{U}$ is determined as 534 ± 7 Ma (MSWD = 0.63, $n = 19$) (Figure 6e,f, Table 3).

In the granitic pegmatite (Z1230-50-1), zircons are observed as granular or columnar, with particle sizes ranging from 100 to 200 μm and a length/width ratio of 1:1–3:1. Cathodoluminescence (CL) images show that some zircon grains exhibit a nucleus–edge structure, featuring a wide inherited nucleus and a slight accretive edge (Figure 5d). Most zircons are lighter, displaying pronounced oscillatory bands and darker edges. A total of 44 U-Pb measurements were conducted on zircon grains, and the $^{206}\text{Pb}/^{238}\text{U}$ and $^{207}\text{Pb}/^{235}\text{U}$ ratios exhibit good concordance (Figure 6g, Table 3). The weighted average age of the $^{206}\text{Pb}/^{238}\text{U}$ peak in the zircon core is 546 ± 6 Ma (MSWD = 0.076, $n = 15$) (Figure 6h). The $^{206}\text{Pb}/^{238}\text{U}$ age of the zircon accretive edge ranges from 463 to 534 Ma, indicating apparent traces of fluid action during later stages, likely representing the new metamorphic edge of pegmatite zircon after the transformation of subsequent thermal events.

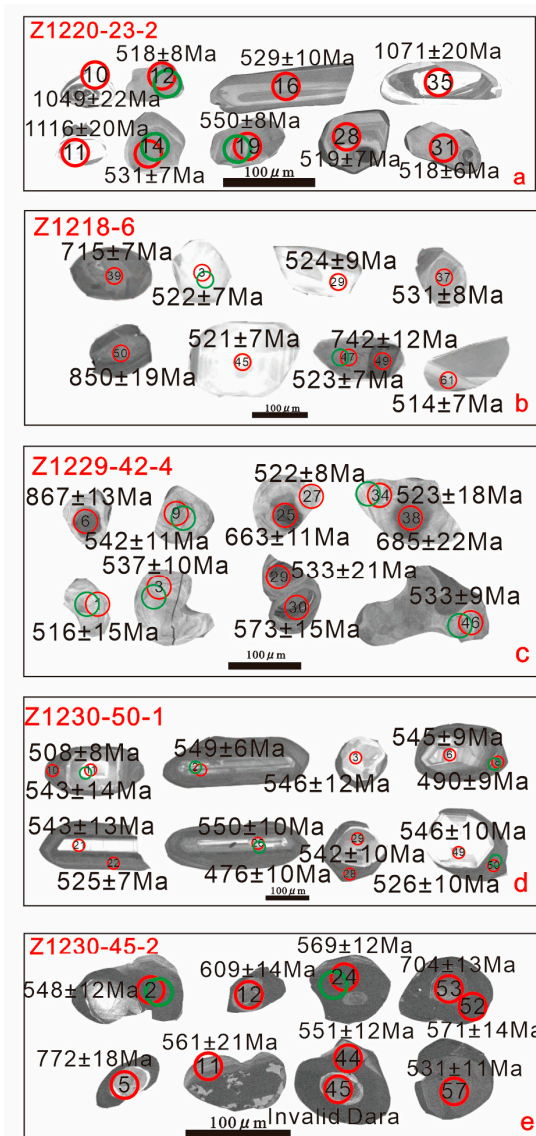


Figure 5. The CL images of representative zircons from the samples (a–e) (The red solid circles represent the U-Pb test points. The green solid circles represent the Hf test points.).

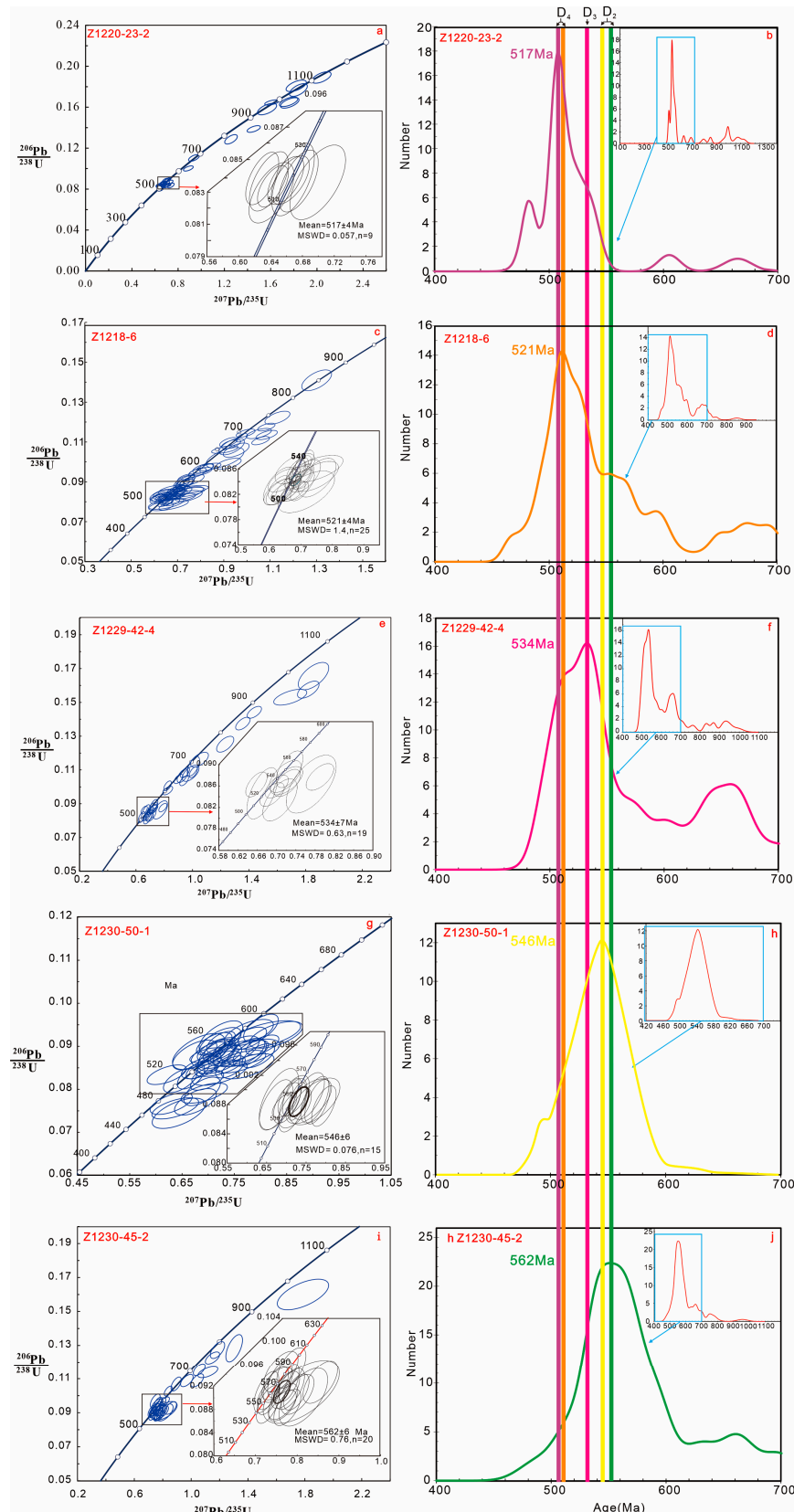


Figure 6. Zircon U-Pb concordia diagrams and age histograms of the (a,b) granitic pegmatite (Z1220-23-2), (c,d) plagioclase pegmatite (Z1218-6), (e,f) the syenite pegmatite (Z1229-42-4), (g,h) the plagioclase pegmatite (Z1230-45-2), and (i,j) the granitic pegmatite (Z1230-50-1).5.2.2. Trace Elements in Zircon.

Table 3. LA-ICP-MS zircon U-Pb data of the samples.

Spots	Th	U	Th/U	$^{207}\text{Pb}/^{206}\text{Pb}$	$^{207}\text{Pb}/^{206}\text{Pb}$	$^{207}\text{Pb}/^{235}\text{U}$	$^{207}\text{Pb}/^{235}\text{U}$	$^{206}\text{Pb}/^{238}\text{U}$	$^{206}\text{Pb}/^{238}\text{U}$	$^{207}\text{Pb}/^{206}\text{Pb}$	$^{207}\text{Pb}/^{206}\text{Pb}$	$^{207}\text{Pb}/^{235}\text{U}$	$^{207}\text{Pb}/^{235}\text{U}$	$^{206}\text{Pb}/^{238}\text{U}$	$^{206}\text{Pb}/^{238}\text{U}$
	ppm	ppm		Ratio	1 σ	Ratio	1 σ	Ratio	1 σ	Age (Ma)	1 σ	Age (Ma)	1 σ	Age (Ma)	1 σ
Z1220-23-2															
3	114.6	985.0	0.1164	0.0623	0.0019	0.6835	0.0259	0.0794	0.0016	687	65	529	16	492	10
4	91.8	438.7	0.2092	0.0586	0.0013	0.6752	0.0163	0.0837	0.0013	554	55	524	10	518	8
5	204.7	652.3	0.3138	0.0608	0.0019	0.6993	0.0230	0.0836	0.0015	632	69	538	14	517	9
7	119.5	449.2	0.2659	0.0562	0.0017	0.6412	0.0186	0.0829	0.0012	461	67	503	12	514	7
8	131.7	134.0	0.9827	0.0782	0.0022	1.7650	0.0530	0.1642	0.0034	1154	57	1033	19	980	19
9	52.9	110.1	0.4799	0.0779	0.0027	1.7552	0.0526	0.1653	0.0031	1146	69	1029	19	986	17
10	571.1	893.4	0.6393	0.0759	0.0019	1.8397	0.0510	0.1768	0.0041	1094	50	1060	18	1050	22
11	102.0	137.5	0.7414	0.0789	0.0023	2.0391	0.0554	0.1890	0.0037	1169	51	1129	19	1116	20
12	104.0	411.7	0.2527	0.0580	0.0014	0.6683	0.0176	0.0838	0.0015	528	56	520	11	519	9
14	123.3	450.9	0.2734	0.0571	0.0013	0.6766	0.0180	0.0859	0.0011	494	52	525	11	531	7
15	117.7	471.1	0.2498	0.0606	0.0015	0.7242	0.0213	0.0867	0.0014	633	56	553	13	536	8
16	243.3	593.9	0.4097	0.0595	0.0013	0.6983	0.0182	0.0855	0.0016	583	16	538	11	529	10
17	323.9	515.9	0.6279	0.0709	0.0014	1.2571	0.0362	0.1287	0.0030	955	36	827	16	780	17
19	192.3	503.6	0.3818	0.0579	0.0012	0.7114	0.0172	0.0891	0.0014	528	46	546	10	550	8
20	153.2	151.0	1.0148	0.0716	0.0017	1.5690	0.0547	0.1582	0.0037	976	47	958	22	947	21
21	133.3	469.6	0.2838	0.0577	0.0011	0.7014	0.0150	0.0883	0.0012	517	43	540	9	545	7
22	208.8	581.0	0.3593	0.0563	0.0013	0.6689	0.0170	0.0862	0.0012	465	55	520	10	533	7
23	20.9	158.5	0.1316	0.0711	0.0019	1.6118	0.0414	0.1647	0.0017	961	54	975	16	983	9
24	111.0	575.5	0.1928	0.0560	0.0012	0.6430	0.0128	0.0833	0.0008	454	46	504	8	516	5
26	137.6	477.4	0.2883	0.0546	0.0011	0.6296	0.0137	0.0838	0.0011	394	44	496	9	519	6
27	68.2	377.8	0.1806	0.0576	0.0013	0.6649	0.0157	0.0837	0.0010	517	44	518	10	518	6
28	135.8	477.6	0.2843	0.0552	0.0010	0.6380	0.0162	0.0836	0.0012	420	34	501	10	518	7
29	100.5	799.0	0.1258	0.0565	0.0010	0.6890	0.0163	0.0884	0.0014	472	39	532	10	546	8
30	89.9	124.1	0.7242	0.0646	0.0019	0.8886	0.0281	0.1002	0.0016	761	64	646	15	615	10
31	160.0	461.7	0.3465	0.0572	0.0013	0.6591	0.0150	0.0837	0.0010	502	50	514	9	518	6
32	114.4	135.5	0.8445	0.0615	0.0016	0.9371	0.0307	0.1105	0.0021	657	50	671	16	676	12
34	79.4	118.8	0.6682	0.0762	0.0019	1.4539	0.0381	0.1387	0.0021	1102	50	912	16	837	12
35	62.4	317.5	0.1965	0.0732	0.0019	1.8212	0.0579	0.1809	0.0037	1020	53	1053	21	1072	20
Z1218-6															
1	185.8	346.9	0.5356	0.0596	0.0014	0.6575	0.0147	0.0799	0.0012	591	50	513	9	496	7
2	75.7	158.6	0.4772	0.0594	0.0016	0.6550	0.0184	0.0798	0.0010	589	59	512	11	495	6
3	146.8	240.5	0.6103	0.0578	0.0012	0.6746	0.0154	0.0845	0.0012	520	46	523	9	523	7
4	71.4	176.1	0.4052	0.0642	0.0017	0.8176	0.0209	0.0923	0.0012	750	52	607	12	569	7
6	15.7	37.7	0.4156	0.0640	0.0040	0.7480	0.0470	0.0848	0.0016	743	132	567	27	525	9
8	44.7	98.5	0.4541	0.0614	0.0019	0.6752	0.0228	0.0797	0.0011	654	67	524	14	494	7
9	158.8	245.5	0.6468	0.0586	0.0015	0.6888	0.0175	0.0855	0.0012	550	53	532	11	529	7
10	100.6	185.4	0.5428	0.0607	0.0012	0.7716	0.0154	0.0923	0.0013	628	75	581	9	569	7
11	33.8	56.3	0.6006	0.0609	0.0029	0.6962	0.0308	0.0835	0.0016	635	101	537	18	517	9

Table 3. Cont.

Spots	Th	U	Th/U	$^{207}\text{Pb}/^{206}\text{Pb}$	$^{207}\text{Pb}/^{206}\text{Pb}$	$^{207}\text{Pb}/^{235}\text{U}$	$^{207}\text{Pb}/^{235}\text{U}$	$^{206}\text{Pb}/^{238}\text{U}$	$^{206}\text{Pb}/^{238}\text{U}$	$^{207}\text{Pb}/^{206}\text{Pb}$	$^{207}\text{Pb}/^{206}\text{Pb}$	$^{207}\text{Pb}/^{235}\text{U}$	$^{207}\text{Pb}/^{235}\text{U}$	$^{206}\text{Pb}/^{238}\text{U}$	$^{206}\text{Pb}/^{238}\text{U}$
	ppm	ppm		Ratio	1σ	Ratio	1σ	Ratio	1σ	Age (Ma)	1σ	Age (Ma)	1σ	Age (Ma)	1σ
12	135.6	285.4	0.4753	0.0606	0.0013	0.7113	0.0191	0.0848	0.0013	633	72	545	11	525	8
13	11.9	26.1	0.4544	0.0568	0.0031	0.7019	0.0391	0.0896	0.0015	483	116	540	23	553	9
14	190.7	258.9	0.7364	0.0589	0.0015	0.7037	0.0194	0.0864	0.0011	565	54	541	12	534	7
15	124.5	180.5	0.6898	0.0577	0.0013	0.7077	0.0163	0.0891	0.0014	517	52	543	10	550	8
16	42.7	97.7	0.4370	0.0575	0.0020	0.6600	0.0263	0.0830	0.0013	509	78	515	16	514	8
18	25.4	50.5	0.5021	0.0557	0.0029	0.6297	0.0314	0.0824	0.0014	439	115	496	20	510	8
19	47.5	104.0	0.4563	0.0552	0.0023	0.6194	0.0254	0.0816	0.0015	420	93	490	16	505	9
20	55.2	116.5	0.4736	0.0606	0.0021	0.8114	0.0303	0.0968	0.0016	628	74	603	17	596	9
21	52.9	121.3	0.4359	0.0647	0.0021	0.9604	0.0362	0.1074	0.0027	765	67	683	19	658	16
22	13.7	31.1	0.4397	0.0553	0.0029	0.6325	0.0344	0.0833	0.0020	433	149	498	21	516	12
23	428.7	1393.1	0.3077	0.0649	0.0009	1.0037	0.0161	0.1119	0.0014	770	28	706	8	684	8
24	60.2	86.8	0.6931	0.0648	0.0025	0.7348	0.0292	0.0823	0.0013	769	86	559	17	510	8
25	77.2	135.3	0.5703	0.0592	0.0016	0.7116	0.0194	0.0872	0.0011	572	61	546	11	539	7
26	38.6	68.3	0.5655	0.0610	0.0026	0.7992	0.0331	0.0951	0.0014	639	91	596	19	586	8
28	151.9	259.7	0.5849	0.0711	0.0015	1.0851	0.0253	0.1104	0.0014	961	43	746	12	675	8
29	127.6	199.4	0.6396	0.0600	0.0016	0.7025	0.0211	0.0848	0.0013	611	58	540	13	525	8
32	12.2	26.2	0.4636	0.0597	0.0045	0.6509	0.0506	0.0790	0.0019	591	163	509	31	490	11
33	99.1	119.7	0.8280	0.0671	0.0021	0.9798	0.0370	0.1057	0.0024	843	65	694	19	648	14
34	31.5	66.2	0.4756	0.0714	0.0023	1.1113	0.0305	0.1133	0.0015	970	65	759	15	692	9
36	57.6	126.0	0.4575	0.0603	0.0020	0.7858	0.0252	0.0947	0.0016	617	70	589	14	583	9
38	136.9	278.8	0.4909	0.0579	0.0016	0.7381	0.0238	0.0920	0.0013	528	61	561	14	568	7
39	260.2	275.5	0.9442	0.0670	0.0016	1.0839	0.0248	0.1175	0.0013	835	51	746	12	716	7
40	16.2	35.7	0.4539	0.0540	0.0038	0.6004	0.0393	0.0819	0.0017	369	155	477	25	507	10
41	165.9	285.8	0.5804	0.0576	0.0015	0.6530	0.0201	0.0819	0.0012	522	59	510	12	508	7
42	59.4	80.5	0.7381	0.0632	0.0025	0.9055	0.0541	0.1021	0.0034	717	83	655	29	627	20
43	102.6	155.4	0.6602	0.0608	0.0017	0.7955	0.0292	0.0948	0.0024	632	66	594	16	584	14
44	58.5	101.0	0.5786	0.0586	0.0020	0.7366	0.0277	0.0911	0.0016	554	77	560	16	562	9
45	20.7	55.8	0.3717	0.0557	0.0028	0.6434	0.0314	0.0842	0.0012	439	111	504	19	521	7
47	152.8	233.4	0.6549	0.0591	0.0024	0.6889	0.0279	0.0847	0.0012	569	87	532	17	524	7
48	77.3	138.2	0.5590	0.0677	0.0028	0.9202	0.0365	0.0991	0.0018	861	86	662	19	609	11
49	81.9	180.2	0.4542	0.0672	0.0018	1.1317	0.0357	0.1221	0.0022	843	56	769	17	743	12
50	194.5	357.0	0.5448	0.0667	0.0012	1.3011	0.0426	0.1410	0.0034	829	44	846	19	850	19
51	96.2	270.7	0.3555	0.0638	0.0016	0.9577	0.0276	0.1087	0.0015	744	54	682	14	665	9
52	20.3	42.4	0.4781	0.0583	0.0039	0.6809	0.0417	0.0861	0.0016	543	146	527	25	532	9
53	101.8	147.4	0.6904	0.0598	0.0014	0.7410	0.0208	0.0898	0.0016	598	55	563	12	554	10
54	80.8	165.5	0.4884	0.0573	0.0018	0.6468	0.0195	0.0820	0.0012	506	69	507	12	508	7
55	170.0	262.6	0.6471	0.0596	0.0014	0.7369	0.0202	0.0895	0.0014	591	20	561	12	553	8
56	115.0	230.5	0.4989	0.0619	0.0013	0.8252	0.0188	0.0967	0.0014	672	42	611	10	595	8
57	123.9	159.8	0.7751	0.0591	0.0017	0.7218	0.0194	0.0890	0.0015	572	63	552	11	549	9
59	45.6	62.7	0.7274	0.0605	0.0028	0.7575	0.0381	0.0910	0.0019	620	102	573	22	561	11
60	72.4	87.4	0.8287	0.0595	0.0022	0.7304	0.0278	0.0891	0.0015	587	80	557	16	550	9

Table 3. Cont.

Spots	Th	U	Th/U	$^{207}\text{Pb}/^{206}\text{Pb}$	$^{207}\text{Pb}/^{206}\text{Pb}$	$^{207}\text{Pb}/^{235}\text{U}$	$^{207}\text{Pb}/^{235}\text{U}$	$^{206}\text{Pb}/^{238}\text{U}$	$^{206}\text{Pb}/^{238}\text{U}$	$^{207}\text{Pb}/^{206}\text{Pb}$	$^{207}\text{Pb}/^{206}\text{Pb}$	$^{207}\text{Pb}/^{235}\text{U}$	$^{207}\text{Pb}/^{235}\text{U}$	$^{206}\text{Pb}/^{238}\text{U}$	$^{206}\text{Pb}/^{238}\text{U}$
	ppm	ppm		Ratio	1σ	Ratio	1σ	Ratio	1σ	Age (Ma)	1σ	Age (Ma)	1σ	Age (Ma)	1σ
61	46.4	112.1	0.4141	0.0551	0.0020	0.6302	0.0223	0.0831	0.0012	417	81	496	14	514	7
62	109.7	211.3	0.5191	0.0563	0.0015	0.6338	0.0167	0.0816	0.0010	465	59	498	10	505	6
63	124.8	313.7	0.3978	0.0578	0.0015	0.6831	0.0191	0.0856	0.0012	524	62	529	12	530	7
64	130.8	209.2	0.6254	0.0626	0.0017	0.9466	0.0256	0.1097	0.0015	694	57	676	13	671	9
66	22.4	30.3	0.7403	0.0653	0.0043	0.8326	0.0553	0.0926	0.0018	783	139	615	31	571	11
67	156.8	244.6	0.6411	0.0585	0.0018	0.6510	0.0187	0.0812	0.0014	546	67	509	12	503	8
68	95.6	147.6	0.6481	0.0636	0.0025	0.9304	0.0377	0.1060	0.0013	728	83	668	20	649	7
70	136.0	275.9	0.4931	0.0612	0.0017	0.6954	0.0191	0.0825	0.0010	656	61	536	11	511	6
71	111.2	233.1	0.4770	0.0593	0.0021	0.6449	0.0203	0.0794	0.0012	576	78	505	13	493	7
72	55.7	126.7	0.4391	0.0573	0.0026	0.6474	0.0287	0.0823	0.0011	502	106	507	18	510	6
73	59.8	115.7	0.5173	0.0669	0.0023	1.0517	0.0360	0.1142	0.0017	835	72	730	18	697	10
75	45.2	109.3	0.4139	0.0561	0.0028	0.6338	0.0297	0.0824	0.0014	457	109	498	18	510	8
76	156.2	376.4	0.4149	0.0588	0.0014	0.6959	0.0181	0.0859	0.0012	567	52	536	11	531	7
77	75.0	128.8	0.5828	0.0649	0.0017	1.0205	0.0270	0.1142	0.0013	770	56	714	14	697	8
78	57.9	132.3	0.4374	0.0612	0.0022	0.6512	0.0206	0.0776	0.0012	656	76	509	13	482	7
79	62.2	147.5	0.4214	0.0595	0.0023	0.6760	0.0251	0.0826	0.0011	587	116	524	15	511	6
80	66.5	87.4	0.7607	0.0623	0.0025	0.8365	0.0343	0.0975	0.0012	683	87	617	19	600	7
81	29.4	71.4	0.4119	0.0636	0.0033	0.6520	0.0340	0.0747	0.0011	728	111	510	21	465	7
Z1230-42-4															
1	95.3	609.7	0.1562	0.0620	0.0017	0.7070	0.0235	0.0834	0.0026	674	60	543	14	516	15
2	92.5	1488.9	0.0621	0.0652	0.0014	0.7392	0.0198	0.0823	0.0022	781	44	562	12	510	13
3	107.4	928.6	0.1156	0.0600	0.0016	0.7208	0.0222	0.0870	0.0017	606	57	551	13	538	10
5	81.9	717.2	0.1142	0.0652	0.0014	1.0492	0.0417	0.1161	0.0029	789	51	729	21	708	17
6	40.8	1388.0	0.0294	0.0724	0.0018	1.4369	0.0337	0.1441	0.0023	998	54	904	14	868	13
8	93.7	936.7	0.1001	0.0624	0.0011	0.9007	0.0205	0.1047	0.0018	687	37	652	11	642	11
9	146.0	671.0	0.2175	0.0591	0.0011	0.7180	0.0218	0.0878	0.0020	572	43	550	13	543	12
10	51.1	4929.3	0.0104	0.0714	0.0012	1.3557	0.0338	0.1374	0.0025	969	36	870	15	830	14
11	131.2	534.6	0.2454	0.0612	0.0016	0.8244	0.0233	0.0978	0.0017	656	57	610	13	602	10
13	25.7	2180.6	0.0118	0.0709	0.0013	1.2310	0.0401	0.1252	0.0031	955	39	815	18	761	18
14	41.9	2646.0	0.0158	0.0633	0.0012	0.9297	0.0255	0.1066	0.0026	717	44	667	13	653	15
16	51.0	2411.9	0.0212	0.0672	0.0010	1.0058	0.0193	0.1086	0.0021	844	31	707	10	665	12
19	25.1	774.8	0.0324	0.0660	0.0015	0.9405	0.0204	0.1036	0.0019	806	42	673	11	636	11
20	75.4	604.4	0.1248	0.0671	0.0017	0.8645	0.0265	0.0933	0.0021	840	56	633	14	575	13
21	114.0	1121.2	0.1016	0.0664	0.0023	0.9864	0.0393	0.1081	0.0032	817	70	697	20	662	18
22	9.3	1249.1	0.0075	0.0809	0.0018	1.8551	0.0713	0.1656	0.0054	1220	43	1065	25	988	30
25	95.2	872.9	0.1091	0.0632	0.0009	0.9464	0.0211	0.1084	0.0020	722	31	676	11	664	12
27	269.0	1076.3	0.2499	0.0591	0.0010	0.6908	0.0166	0.0844	0.0015	572	5	533	10	523	9
28	74.3	723.3	0.1028	0.0658	0.0020	0.7368	0.0248	0.0823	0.0028	798	58	561	15	510	17
29	8.5	1024.2	0.0083	0.0653	0.0023	0.7719	0.0342	0.0864	0.0036	787	73	581	20	534	21
30	175.9	925.9	0.1899	0.0574	0.0013	0.7322	0.0208	0.0930	0.0026	506	55	558	12	573	15

Table 3. Cont.

Spots	Th	U	Th/U	$^{207}\text{Pb}/^{206}\text{Pb}$	$^{207}\text{Pb}/^{206}\text{Pb}$	$^{207}\text{Pb}/^{235}\text{U}$	$^{207}\text{Pb}/^{235}\text{U}$	$^{206}\text{Pb}/^{238}\text{U}$	$^{206}\text{Pb}/^{238}\text{U}$	$^{207}\text{Pb}/^{206}\text{Pb}$	$^{207}\text{Pb}/^{206}\text{Pb}$	$^{207}\text{Pb}/^{235}\text{U}$	$^{207}\text{Pb}/^{235}\text{U}$	$^{206}\text{Pb}/^{238}\text{U}$	$^{206}\text{Pb}/^{238}\text{U}$
	ppm	ppm		Ratio	1σ	Ratio	1σ	Ratio	1σ	Age (Ma)	1σ	Age (Ma)	1σ	Age (Ma)	1σ
Z1230-50-1															
2	33.3	969.1	0.0344	0.0581	0.0008	0.7145	0.0161	0.0890	0.0017	532	30	547	10	550	10
3	773.3	191.2	4.0453	0.0623	0.0022	0.7724	0.0419	0.0884	0.0021	683	79	581	24	546	13
4	600.4	277.6	2.1626	0.0613	0.0016	0.7760	0.0232	0.0918	0.0017	650	56	583	13	566	10
5	522.2	258.8	2.0176	0.0573	0.0016	0.6956	0.0207	0.0879	0.0011	502	63	536	12	543	7
6	65.8	756.5	0.0870	0.0638	0.0012	0.7788	0.0212	0.0884	0.0020	744	38	585	12	546	12
7	455.3	305.3	1.4910	0.0626	0.0025	0.6432	0.0335	0.0744	0.0023	694	85	504	21	463	14
8	421.5	173.6	2.4276	0.0633	0.0023	0.6919	0.0293	0.0791	0.0015	717	76	534	18	491	9
9	29.8	1063.2	0.0280	0.0633	0.0014	0.7418	0.0187	0.0852	0.0017	717	46	563	11	527	10
10	432.1	145.6	2.9674	0.0618	0.0018	0.6973	0.0210	0.0821	0.0015	733	62	537	13	508	9
11	83.5	821.2	0.1017	0.0590	0.0011	0.7160	0.0240	0.0879	0.0024	565	41	548	14	543	14
12	21.5	1260.1	0.0171	0.0610	0.0024	0.6366	0.0295	0.0755	0.0016	639	83	500	18	469	10
13	205.7	190.4	1.0805	0.0655	0.0021	0.7751	0.0332	0.0853	0.0019	791	66	583	19	528	11
15	461.8	248.3	1.8597	0.0573	0.0017	0.7238	0.0275	0.0920	0.0025	502	65	553	16	568	15
16	16.6	685.5	0.0242	0.0594	0.0010	0.7019	0.0148	0.0859	0.0016	589	39	540	9	531	9
17	325.5	120.7	2.6973	0.0613	0.0024	0.7208	0.0274	0.0862	0.0017	650	83	551	16	533	10
18	334.2	561.5	0.5953	0.0635	0.0020	0.6752	0.0264	0.0771	0.0020	724	69	524	16	479	12
20	243.7	91.0	2.6771	0.0653	0.0026	0.8290	0.0335	0.0926	0.0021	783	85	613	19	571	12
21	222.5	102.6	2.1681	0.0555	0.0018	0.6738	0.0279	0.0880	0.0023	432	69	523	17	543	13
22	287.8	94.3	3.0503	0.0612	0.0022	0.7174	0.0282	0.0849	0.0013	656	76	549	17	525	8
23	35.2	900.8	0.0391	0.0628	0.0015	0.6880	0.0231	0.0795	0.0022	702	52	532	14	493	13
24	191.8	337.3	0.5686	0.0607	0.0021	0.7772	0.0309	0.0931	0.0020	628	76	584	18	574	12
26	434.6	148.7	2.9229	0.0589	0.0022	0.7183	0.0261	0.0892	0.0018	565	80	550	15	551	11
27	39.8	1033.5	0.0385	0.0585	0.0012	0.6668	0.0173	0.0829	0.0019	546	44	519	11	513	11
28	141.7	142.9	0.9912	0.0602	0.0030	0.6289	0.0266	0.0767	0.0017	613	107	495	17	476	10
29	953.5	386.4	2.4681	0.0658	0.0014	0.7952	0.0205	0.0878	0.0018	1200	51	594	12	542	11

Table 3. Cont.

Spots	Th	U	Th/U	$^{207}\text{Pb}/^{206}\text{Pb}$	$^{207}\text{Pb}/^{206}\text{Pb}$	$^{207}\text{Pb}/^{235}\text{U}$	$^{207}\text{Pb}/^{235}\text{U}$	$^{206}\text{Pb}/^{238}\text{U}$	$^{206}\text{Pb}/^{238}\text{U}$	$^{207}\text{Pb}/^{206}\text{Pb}$	$^{207}\text{Pb}/^{206}\text{Pb}$	$^{207}\text{Pb}/^{235}\text{U}$	$^{207}\text{Pb}/^{235}\text{U}$	$^{206}\text{Pb}/^{238}\text{U}$	$^{206}\text{Pb}/^{238}\text{U}$
	ppm	ppm		Ratio	1σ	Ratio	1σ	Ratio	1σ	Age (Ma)	1σ	Age (Ma)	1σ	Age (Ma)	1σ
30	160.5	261.0	0.6150	0.0619	0.0021	0.7563	0.0266	0.0892	0.0021	672	72	572	15	551	13
31	235.5	159.3	1.4788	0.0573	0.0017	0.6461	0.0212	0.0820	0.0019	506	65	506	13	508	11
33	273.4	199.8	1.3679	0.0571	0.0017	0.7111	0.0225	0.0906	0.0017	494	67	545	13	559	10
34	148.3	293.0	0.5062	0.0574	0.0015	0.7227	0.0263	0.0910	0.0022	506	57	552	16	561	13
35	319.2	108.2	2.9513	0.0647	0.0024	0.8896	0.0280	0.1020	0.0031	765	79	646	15	626	18
36	153.5	1062.0	0.1445	0.0616	0.0012	0.8003	0.0219	0.0942	0.0021	661	43	597	12	580	13
37	549.1	147.2	3.7311	0.0544	0.0023	0.6202	0.0247	0.0834	0.0015	387	96	490	15	516	9
38	42.4	1128.3	0.0376	0.0620	0.0023	0.7210	0.0348	0.0837	0.0019	674	78	551	21	518	11
39	425.8	119.2	3.5726	0.0630	0.0032	0.8078	0.0450	0.0926	0.0022	709	107	601	25	571	13
40	108.8	1002.6	0.1085	0.0643	0.0016	0.8029	0.0208	0.0903	0.0015	754	249	598	12	557	9
41	410.6	130.6	3.1444	0.0596	0.0020	0.7223	0.0274	0.0876	0.0018	591	70	552	16	541	11
42	380.0	277.8	1.3682	0.0576	0.0015	0.7019	0.0230	0.0882	0.0018	522	57	540	14	545	11
43	98.7	1048.1	0.0942	0.0629	0.0012	0.7722	0.0234	0.0887	0.0021	702	39	581	13	548	12
44	52.5	1179.3	0.0446	0.0632	0.0020	0.7604	0.0325	0.0864	0.0017	717	63	574	19	534	10
45	42.1	1078.4	0.0391	0.0582	0.0011	0.6793	0.0146	0.0844	0.0013	539	45	526	9	522	8
46	160.0	1000.8	0.1599	0.0575	0.0011	0.7237	0.0181	0.0909	0.0017	522	39	553	11	561	10
47	333.1	157.4	2.1168	0.0615	0.0027	0.7567	0.0382	0.0884	0.0020	657	92	572	22	546	12
48	244.2	99.2	2.4621	0.0556	0.0022	0.6813	0.0331	0.0888	0.0028	435	87	528	20	548	16
49	25.1	1035.9	0.0242	0.0598	0.0013	0.7271	0.0154	0.0884	0.0017	594	44	555	9	546	10
50	513.3	162.4	3.1598	0.0584	0.0019	0.6873	0.0258	0.0850	0.0017	546	72	531	16	526	10
Z1230-45-2															
1	96.2	601.8	0.1598	0.0655	0.0023	0.8150	0.0383	0.0901	0.0033	791	70	605	21	556	20
2	36.2	2220.2	0.0163	0.0600	0.0014	0.7305	0.0185	0.0889	0.0022	611	48	557	11	549	13
3	195.3	1026.2	0.1903	0.0573	0.0012	0.6644	0.0149	0.0844	0.0016	502	46	517	9	523	10
5	287.3	478.5	0.6005	0.0678	0.0015	1.1851	0.0334	0.1273	0.0033	865	46	794	16	773	19
6	137.0	966.7	0.1417	0.0652	0.0025	0.8012	0.0258	0.0906	0.0023	789	80	598	15	559	13
9	55.3	1587.2	0.0348	0.0694	0.0024	1.0308	0.0478	0.1072	0.0027	909	76	719	24	656	16
11	19.2	1248.7	0.0154	0.0641	0.0035	0.8099	0.0602	0.0911	0.0036	744	112	602	34	562	21
12	481.6	842.8	0.5714	0.0689	0.0020	0.9402	0.0323	0.0992	0.0025	894	59	673	17	610	14
13	351.2	642.1	0.5470	0.0743	0.0028	1.3025	0.0385	0.1284	0.0053	1050	77	847	17	779	30
14	88.0	415.4	0.2118	0.0614	0.0016	0.8943	0.0237	0.1068	0.0027	654	56	649	13	654	16
15	73.9	351.3	0.2102	0.0565	0.0016	0.7473	0.0229	0.0970	0.0026	478	63	567	13	597	16
17	278.9	335.0	0.8327	0.0799	0.0031	1.7867	0.1192	0.1600	0.0059	1195	77	1041	43	957	33
18	101.0	1962.1	0.0515	0.0612	0.0014	0.7723	0.0224	0.0914	0.0021	648	48	581	13	564	13
19	138.3	382.8	0.3614	0.0611	0.0015	0.8144	0.0217	0.0967	0.0017	643	54	605	12	595	10
20	116.2	718.4	0.1617	0.0694	0.0016	1.0429	0.0297	0.1090	0.0025	910	52	725	15	667	15
21	345.0	545.8	0.6320	0.0645	0.0016	0.9699	0.0291	0.1089	0.0024	767	52	688	15	666	14
22	288.4	605.1	0.4766	0.0676	0.0015	1.1497	0.0332	0.1226	0.0024	857	46	777	16	746	14
23	45.5	3417.5	0.0133	0.0578	0.0010	0.7265	0.0197	0.0910	0.0024	520	42	555	12	561	14
24	33.9	3659.8	0.0093	0.0586	0.0011	0.7492	0.0200	0.0923	0.0021	554	36	568	12	569	12

Table 3. Cont.

Spots	Th	U	Th/U	$^{207}\text{Pb}/^{206}\text{Pb}$	$^{207}\text{Pb}/^{206}\text{Pb}$	$^{207}\text{Pb}/^{235}\text{U}$	$^{207}\text{Pb}/^{235}\text{U}$	$^{206}\text{Pb}/^{238}\text{U}$	$^{206}\text{Pb}/^{238}\text{U}$	$^{207}\text{Pb}/^{206}\text{Pb}$	$^{207}\text{Pb}/^{206}\text{Pb}$	$^{207}\text{Pb}/^{235}\text{U}$	$^{207}\text{Pb}/^{235}\text{U}$	$^{206}\text{Pb}/^{238}\text{U}$	$^{206}\text{Pb}/^{238}\text{U}$
	ppm	ppm		Ratio	1σ	Ratio	1σ	Ratio	1σ	Age (Ma)	1σ	Age (Ma)	1σ	Age (Ma)	1σ
25	81.5	421.4	0.1934	0.0638	0.0016	0.7767	0.0214	0.0883	0.0021	744	52	584	12	546	12
26	44.7	4226.8	0.0106	0.0596	0.0011	0.7864	0.0229	0.0952	0.0024	587	41	589	13	587	14
27	52.7	2809.1	0.0187	0.0613	0.0012	0.7803	0.0162	0.0927	0.0021	650	47	586	9	571	13
28	108.0	938.7	0.1150	0.0634	0.0014	0.7723	0.0209	0.0879	0.0016	724	46	581	12	543	9
29	96.7	220.4	0.4387	0.0589	0.0017	0.7525	0.0243	0.0925	0.0019	565	65	570	14	570	11
30	44.2	2711.2	0.0163	0.0632	0.0013	0.7625	0.0156	0.0874	0.0016	717	47	575	9	540	9
31	53.9	1525.3	0.0354	0.0578	0.0012	0.6945	0.0162	0.0869	0.0015	520	44	535	10	537	9
32	61.8	1216.0	0.0508	0.0582	0.0012	0.7072	0.0188	0.0877	0.0017	600	44	543	11	542	10
33	304.3	1711.8	0.1778	0.0706	0.0023	1.1169	0.0464	0.1139	0.0022	946	67	762	22	695	13
34	34.4	3714.3	0.0093	0.0579	0.0012	0.7686	0.0184	0.0962	0.0019	524	44	579	11	592	11
35	148.5	518.2	0.2865	0.0570	0.0013	0.6814	0.0188	0.0866	0.0018	500	52	528	11	536	11
36	164.1	603.4	0.2720	0.0590	0.0014	0.6986	0.0193	0.0857	0.0015	565	47	538	12	530	9
38	45.9	3938.2	0.0117	0.0623	0.0012	0.7650	0.0219	0.0887	0.0018	687	43	577	13	548	10
39	117.8	377.5	0.3122	0.0580	0.0012	0.7615	0.0270	0.0946	0.0024	532	46	575	16	583	14
40	71.2	6465.7	0.0110	0.0592	0.0011	0.8382	0.0185	0.1027	0.0019	576	8	618	10	630	11
42	286.6	584.7	0.4901	0.0680	0.0022	0.9720	0.0513	0.1025	0.0031	878	101	690	26	629	18
43	32.7	3076.5	0.0106	0.0622	0.0012	0.7830	0.0228	0.0916	0.0024	680	41	587	13	565	14
44	54.7	2697.7	0.0203	0.0624	0.0015	0.7664	0.0232	0.0894	0.0021	687	52	578	13	552	12
47	24.8	2720.1	0.0091	0.0639	0.0012	0.7982	0.0200	0.0910	0.0021	739	45	596	11	561	12
49	35.4	3761.1	0.0094	0.0592	0.0011	0.7589	0.0195	0.0933	0.0022	572	6	573	11	575	13
50	122.4	705.4	0.1735	0.0593	0.0012	0.7319	0.0174	0.0899	0.0019	589	10	558	10	555	11
52	45.0	2438.6	0.0185	0.0669	0.0014	0.8554	0.0273	0.0928	0.0025	835	43	628	15	572	14
53	124.0	539.7	0.2298	0.0663	0.0010	1.0573	0.0277	0.1155	0.0024	817	33	732	14	704	14
55	34.4	3303.4	0.0104	0.0585	0.0009	0.7315	0.0174	0.0906	0.0017	550	31	557	10	559	10
57	161.5	838.9	0.1925	0.0591	0.0010	0.6990	0.0179	0.0859	0.0019	569	37	538	11	531	12

Most of the zircons found in the plagioclase pegmatite (Z1230-45-2) exhibit a round shape, with sizes ranging from approximately 80 to 150 μm . Cathodoluminescence (CL) images reveal that the oscillating bands of zircons are not clearly apparent, and inclusions are developed in most zircon cores. The color of the core is lighter, while the color of neogenic zircons is darker. The images indicate signs of fluid alteration during and after the crystallization of zircons (Figure 5e). A total of 44 U-Pb measurements were performed on zircon grains. The concentrated age of new magmatic zircons without Pb loss is 562 ± 6 Ma (MSWD = 0.076, $n = 20$) (Figure 6i,j, Table 3). The zircon core exhibits a beaded age distribution, suggesting that the zircon core was influenced by the superposition of late tectonic-thermal events. This influence is primarily attributed to varying degrees of resetting from both the Pan-African tectonic-thermal events and Grenville tectonic-thermal events.

All the zircons of the five samples (ΣREE , ppm) exhibit LREE depletion and the left-dip characteristics of HREE enrichment (Figure 7a–e). The majority of surveyed sites have zircons that display obvious negative Eu anomalies and positive Ce anomalies, and most have test data with Th/U values between 0.1 and 1 (Table 4), indicative of magmatic zircon characteristics. In the zircon-type discrimination diagram, most zircons within the pegmatites fall within the range associated with magmatic zircons–alteration zircons (Figure 8a,b) [67].

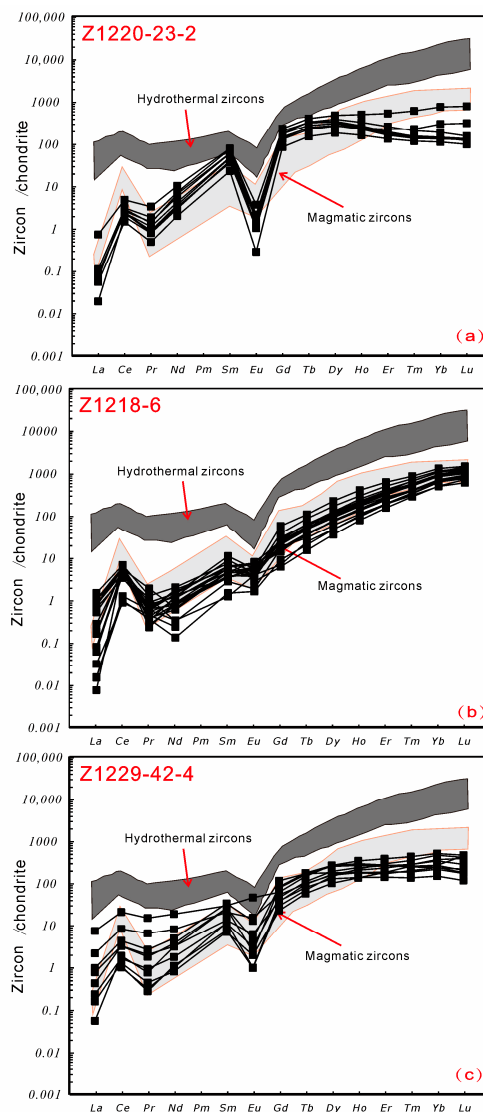


Figure 7. Cont.

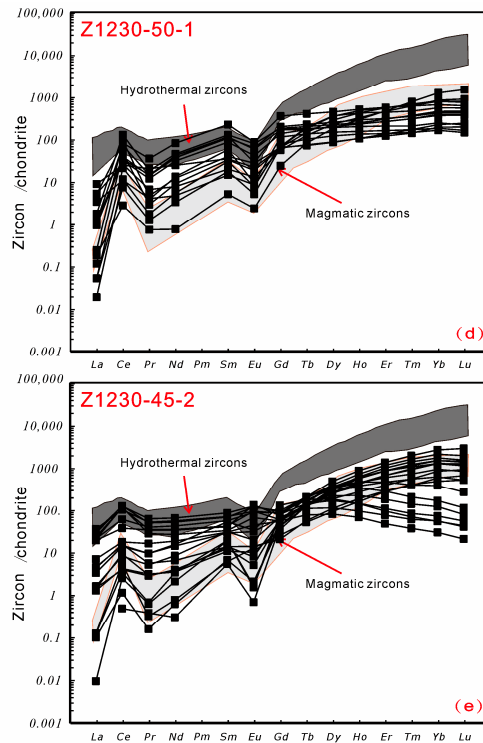


Figure 7. Chondrite-normalized REE patterns (normalization values after Sun and McDonough, 1989 [63] and Hoskin, 2005 [68]) of the new magmatic zircons from the samples. (a) Z1220-23-2; (b) Z1218-6; (c) Z1229-42-4; (d) Z1230-50-1; (e) Z1230-45-2.

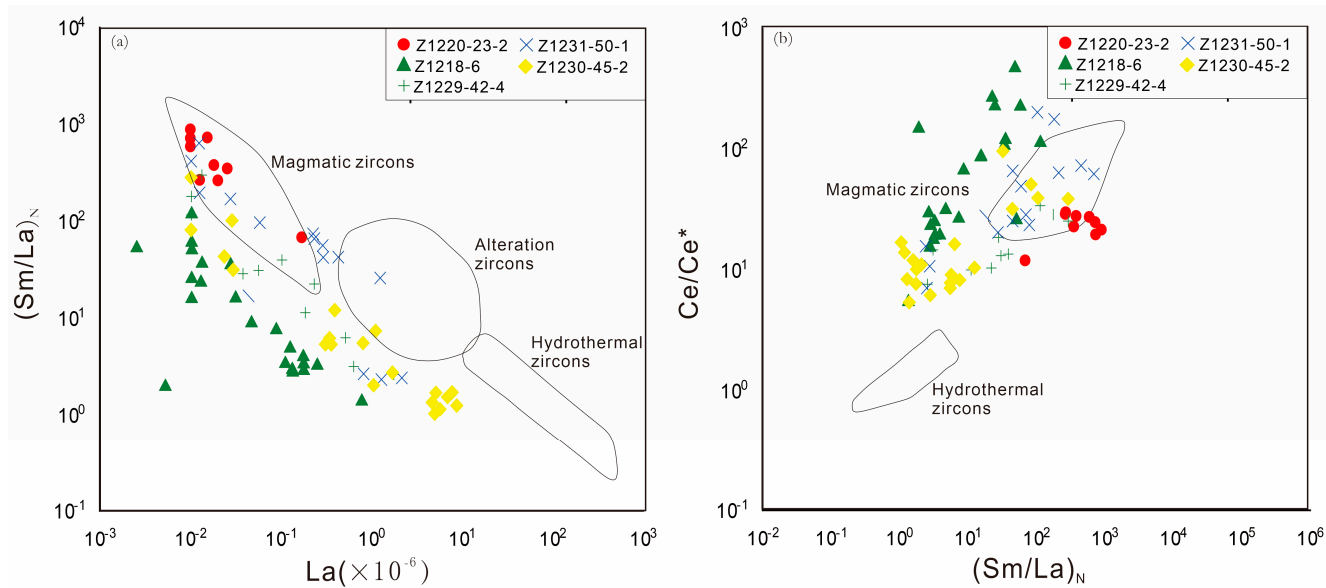


Figure 8. Discriminant diagrams of zircons for pegmatites in the Larsemann Hills in (a,b) [67].

Table 4. Zircon trace and REE ($\times 10^{-6}$) analysis results for the pegmatites.

Spots	Th	U	Th/U	La	Ce	Pr	Nd	Sm	Eu	Gd	Tb	Dy	Ho	Er	Tm	Yb	Lu	Y	Nb	Hf	Ta	Σ REE	LREE	HREE	LREE/ HREE	δ Eu	δ Ce
Z1220-23-2																											
4	91.8	438.7	0.2092	0.01	1.15	0.07	1.35	5.93	0.06	27.52	9.10	67.64	12.76	27.88	3.45	23.15	2.98	395.48	1.30	12,459.67	0.53	183.04	8.57	174.47	0.05	0.01	15.63
5	204.7	652.3	0.3138	0.17	2.87	0.31	4.67	11.60	0.21	46.34	14.69	118.68	27.62	85.47	15.07	125.12	19.43	871.32	2.29	11,319.99	0.93	472.26	19.83	452.43	0.04	0.03	3.08
7	119.5	449.2	0.2659	0.01	1.42	0.10	1.93	7.20	0.06	29.31	8.85	68.00	12.35	25.97	3.37	21.99	3.10	380.54	1.26	11,882.43	0.51	183.65	10.72	172.93	0.06	0.01	
12	104	411.7	0.2527	0.02	1.41	0.08	1.50	5.32	0.07	25.78	8.12	66.11	13.28	35.92	5.62	49.45	7.71	427.32	1.61	12,807.29	0.66	220.39	8.40	211.98	0.04	0.02	8.80
24	111	575.5	0.1928	0.02	1.43	0.08	1.66	6.93	0.10	35.44	12.11	95.80	18.14	41.82	5.13	31.26	3.80	592.94	1.77	13,645.61	0.89	253.72	10.22	243.50	0.04	0.02	8.98
26	137.6	477.4	0.2883	0.03	1.75	0.13	3.01	8.99	0.11	40.35	11.96	86.32	14.82	31.44	3.76	23.76	2.97	486.74	1.56	12,736.93	0.58	229.40	14.01	215.39	0.07	0.02	7.52
27	68.2	377.8	0.1806	0.01	0.88	0.05	0.92	3.39	0.02	16.90	5.51	45.30	8.90	21.33	2.90	18.43	2.44	286.98	1.22	13,837.74	0.53	126.98	5.26	121.71	0.04	0.01	8.95
28	135.8	477.6	0.2843	0.01	1.56	0.13	2.57	8.87	0.06	34.80	10.14	74.74	13.25	28.27	3.50	23.11	2.98	428.65	1.42	12,766.57	0.59	204.00	13.20	190.80	0.07	0.01	0.73
31	160	461.7	0.3465	0.02	1.86	0.17	3.32	11.28	0.12	41.35	11.68	81.62	14.04	29.66	3.82	23.93	3.29	458.63	1.39	13,047.11	0.52	226.16	16.77	209.39	0.08	0.02	8.82
Z1218-6																											
3	146.77	240.47	0.61	0.11	1.42	0.04	0.25	0.36	0.24	2.00	0.97	13.00	5.20	28.39	7.20	83.97	15.94	180.37	0.31	7853.54	0.16	159.10	2.42	156.68	0.02	0.86	5.18
6	15.67	37.70	0.42	0.03	2.57	0.02	0.40	0.94	0.18	5.45	2.23	29.49	11.62	57.72	13.26	135.69	22.87	395.34	0.41	10,255.56	0.33	282.47	4.14	278.33	0.01	0.24	25.96
9	158.82	245.53	0.65	0.05	2.07	0.02	0.25	0.40	0.15	2.94	1.21	17.27	7.10	36.98	8.98	100.76	19.27	241.55	0.49	8626.94	0.40	197.44	2.94	194.51	0.02	0.41	18.06
11	33.83	56.32	0.60	0.24	2.87	0.08	0.66	0.78	0.14	4.24	1.59	21.61	8.52	41.28	9.36	99.63	17.47	284.17	0.47	9814.07	0.41	208.47	4.77	203.70	0.02	0.23	4.92
12	135.65	285.36	0.48	0.75	3.27	0.47	2.55	1.03	0.12	1.98	0.60	9.33	4.31	24.96	6.67	83.69	18.05	144.99	0.34	9271.08	0.25	157.79	8.19	149.60	0.05	0.25	1.36
14	190.67	258.92	0.74	0.13	2.58	0.05	0.43	0.36	0.23	2.23	0.90	13.68	5.63	27.74	7.26	81.93	15.09	186.91	0.26	8413.33	0.35	158.23	3.77	154.46	0.02	0.78	8.09
16	42.72	97.74	0.44	0.01	2.14	0.02	0.26	0.47	0.19	3.23	1.26	16.95	7.07	35.78	9.18	101.17	19.35	233.79	0.52	10,150.70	0.62	197.09	3.10	193.99	0.02	0.46	30.05
18	25.35	50.49	0.50	0.12	2.30	0.03	0.37	0.59	0.14	4.30	1.62	22.02	9.75	47.57	11.66	124.94	22.50	320.94	0.50	11,534.19	0.64	247.91	3.55	244.37	0.01	0.26	9.92
22	13.69	31.14	0.44	0.01	2.70	0.04	0.46	1.17	0.22	8.16	2.80	39.33	15.76	71.50	15.25	153.99	25.82	490.56	1.00	10,439.30	0.83	337.20	4.58	332.61	0.01	0.22	96.23
25	77.16	135.30	0.57	0.13	1.88	0.04	0.29	0.37	0.17	2.65	0.77	10.44	4.32	21.78	5.39	58.63	10.66	141.18	0.31	9228.96	0.26	117.52	2.89	114.63	0.03	0.53	6.84
29	127.57	199.44	0.64	0.17	2.19	0.06	0.47	0.68	0.30	3.58	1.26	18.21	7.33	38.32	9.13	102.77	18.50	244.88	0.32	9840.19	0.13	202.97	3.87	199.10	0.02	0.59	5.35
30	12.16	26.23	0.46	0.09	1.70	0.04	0.52	0.64	0.28	2.43	1.00	12.89	5.23	27.10	6.84	77.78	14.55	185.68	0.25	9047.11	0.21	151.08	3.27	147.81	0.02	0.67	6.82
45	20.74	55.79	0.37	0.01	2.81	0.02	0.28	0.60	0.13	3.78	1.68	20.57	8.51	43.34	10.09	101.36	18.27	277.16	0.67	11,874.08	0.70	211.44	3.83	207.60	0.02	0.27	
47	152.85	233.39	0.65	0.17	1.71	0.05	0.39	0.49	0.32	3.31	1.34	19.20	7.81	41.40	10.18	111.93	21.70	258.06	0.32	10,556.61	0.34	219.99	3.13	216.86	0.01	0.77	4.38
52	20.27	42.40	0.48	0.17	2.60	0.04	0.58	0.57	0.16	3.53	1.24	16.00	6.61	31.99	7.16	74.79	13.30	215.07	0.32	10,043.36	0.33	158.74	4.12	154.62	0.03	0.35	7.80
61	46.44	112.15	0.41	0.01	1.66	0.00	0.10	0.29	0.07	2.35	0.93	13.03	5.74	30.22	7.27	80.66	15.59	189.64	0.58	10,171.51	0.69	157.95	2.15	155.80	0.01	0.28	13.30
63	124.80	313.72	0.40	0.01	0.37	0.00	0.08	0.01	0.11	0.87	0.39	6.24	3.07	17.60	4.99	59.22	12.63	104.65	0.23	8413.70	0.15	105.59	0.57	105.02	0.01	0.21	7.37
70	136.03	275.86	0.49	0.00	0.53	0.04	0.11	0.13	0.16	0.98	0.62	8.39	3.70	21.27	5.89	73.05	15.15	128.90	0.27	10,934.09	1.07	130.01	0.97	129.04	0.01	1.36	13.20
72	55.65	126.74	0.44	0.03	2.41	0.03	0.20	0.49	0.24	3.53	1.46	20.94	8.74	43.62	11.80	126.13	25.31	291.27	0.56	10,539.55	0.77	244.92	3.39	241.53	0.01	0.57	21.06
75	45.24	109.30	0.41	0.01	2.32	0.00	0.21	0.50	0.22	3.72	1.23	18.09	7.30	38.51	9.86	106.69	21.22	245.95	0.63	10,715.34	0.80	209.89	3.26	206.62	0.02	0.48	16.04
76	156.15	376.39	0.41	0.01	0.42	0.00	0.04	0.16	0.06	1.28	0.53	8.29	3.96	22.51	6.14	73.72	16.23	130.49	0.13	9832.89	0.13	133.37	0.69	132.68	0.01	0.44	13.58
79	62.16	147.49	0.42	0.01	1.24	0.00	0.00	0.25	0.06	1.27	0.70	10.10	4.12	22.21	5.65	68.95	12.96	141.20	0.38	10,409.56	0.54	127.52	1.56	125.96	0.01	0.33	0.69
Z1229-42-4																											
1	95.26	609.69	0.16	0.18	1.97	0.19	1.46	2.04	0.35	7.80	2.95	32.40	7.76	23.05	3.43	25.25	2.96	252.29	1.64	14,910.14	0.36	111.82	6.20	105.61	0.06	0.27	2.60
3	107.40	928.63	0.12	0.23	2.61	0.25	2.27	5.05	0.73	23.57	6.29	45.58	9.98	27.72	5.10	40.12	5.48	300.34	0.47	14,425.48	0.36	174.99	11.15	163.85	0.07	0.21	2.69
9	145.96	670.98	0.22	0.01	1.15	0.07	1.44	3.86	0.13	15.93	6.05	63.68	14.95	43.80	6.19	40.54	4.53	492.09	1.82	13,612.56	0.47	202.34	6.67	195.67	0.03	0.05	9.21
27	268.98	1076.28	0.25	0.10	1.93	0.17	1.72	3.93	0.27	17.04	6.56	66.60	16.48	44.77	6.46	45.09	5.13	518.35	2.71	14,957.96	0.89	216.25	8.12	208.13	0.04	0.10	3.64
29	8.48	1024.15	0.01	0.62	8.64	0.49	2.70	1.95	1.00	9.23	4.84	89.91	41.33	245.53	75.97												

Table 4. Cont.

Spots	Th	U	Th/U	La	Ce	Pr	Nd	Sm	Eu	Gd	Tb	Dy	Ho	Er	Tm	Yb	Lu	Y	Nb	Hf	Ta	Σ REE	LREE	HREE	LREE/ HREE	δ Eu	δ Ce
Z1230-50-1																											
2	33.30	969.08	0.03	0.80	6.79	0.39	2.22	2.23	0.50	14.14	7.27	90.31	23.87	72.38	11.87	94.27	13.96	741.31	1.49	12,742.33	1.24	340.98	12.93	328.05	0.04	0.27	2.99
3	773.27	191.15	4.05	0.42	78.96	1.76	21.27	19.54	4.60	37.65	7.52	56.27	13.96	49.45	9.35	77.96	11.76	408.52	1.32	9634.46	0.35	390.47	126.55	263.92	0.48	0.52	22.46
5	522.22	258.84	2.02	0.22	20.72	1.41	17.43	18.00	1.66	35.46	6.78	48.44	11.33	34.24	5.27	41.58	5.57	325.36	0.95	10,491.42	0.32	248.11	59.43	188.68	0.31	0.20	9.09
6	65.78	756.49	0.09	2.12	15.29	1.96	11.60	5.38	1.27	13.31	5.44	72.10	23.77	92.02	17.21	137.66	19.99	747.49	1.11	12,305.58	2.03	419.12	37.62	381.50	0.10	0.46	1.84
11	83.53	821.16	0.10	0.01	4.50	0.12	1.55	2.71	0.30	13.74	6.87	88.39	26.95	94.18	15.73	112.19	15.86	865.69	1.94	12,240.86	1.27	383.11	9.19	373.92	0.02	0.15	28.97
21	222.49	102.62	2.17	0.03	29.85	0.28	4.26	5.12	1.07	12.99	2.80	22.06	5.96	20.01	3.57	32.97	4.97	174.73	0.90	9904.65	0.33	145.93	40.60	105.33	0.39	0.40	84.18
26	434.65	148.70	2.92	0.23	24.22	1.33	17.39	16.51	3.68	41.03	8.45	64.12	16.31	51.58	8.93	72.25	10.98	437.18	1.53	8874.09	0.53	337.00	63.36	273.63	0.23	0.43	10.75
29	953.54	386.35	2.47	1.22	50.43	3.37	38.13	34.28	5.00	72.99	15.03	113.67	28.94	93.68	16.06	133.89	18.98	831.19	1.67	9442.87	0.59	625.68	132.43	493.25	0.27	0.31	6.09
30	160.55	261.05	0.62	0.01	7.05	0.17	2.58	4.67	0.45	15.89	3.80	30.70	7.57	22.66	3.73	27.82	3.67	241.71	1.03	11,693.20	0.56	130.76	14.92	115.84	0.13	0.16	63.21
41	410.59	130.58	3.14	0.28	44.53	1.38	19.48	17.39	3.41	34.73	6.42	50.80	13.45	43.36	7.81	62.23	9.40	370.72	0.91	8992.53	0.36	314.67	86.47	228.20	0.38	0.42	17.47
42	380.01	277.75	1.37	0.01	12.91	0.37	6.26	8.84	0.54	23.43	5.05	37.65	8.73	26.69	4.32	31.02	4.13	262.81	1.40	10,809.46	0.51	169.93	28.93	141.00	0.21	0.12	47.21
43	98.70	1048.06	0.09	1.26	15.93	0.63	3.64	3.07	0.76	11.48	4.66	58.06	18.34	75.76	15.69	143.76	22.83	550.80	2.43	11,817.06	1.84	375.87	25.29	350.58	0.07	0.39	4.37
47	333.09	157.35	2.12	0.29	19.50	1.14	14.65	13.21	2.41	28.22	6.36	50.78	13.06	43.89	7.80	66.44	9.88	365.80	1.90	8342.74	0.53	277.64	51.19	226.45	0.23	0.38	8.37
48	244.15	99.16	2.46	0.06	56.78	0.45	5.76	6.09	1.60	13.51	2.69	21.65	6.01	22.10	4.34	37.76	6.11	182.11	0.72	9189.56	0.23	184.92	70.75	114.17	0.62	0.54	86.80
49	25.11	1035.92	0.02	0.04	1.70	0.07	0.35	0.79	0.14	4.95	3.07	46.18	16.76	77.58	19.73	213.69	38.07	567.60	1.60	11,485.24	1.92	423.11	3.09	420.02	0.01	0.21	7.61
Z1230-45-2																											
1	96.20	601.80	0.16	0.78	8.53	0.91	6.66	4.40	1.79	13.38	4.90	46.60	15.20	64.38	14.09	142.74	23.52	65.19	1.99	11,780.76	1.37	347.89	23.08	324.81	0.07	0.71	2.48
2	36.20	2220.20	0.02	1.66	10.88	1.55	8.64	4.61	2.57	11.18	4.78	54.98	12.71	29.86	3.54	20.55	2.00	58.70	1.12	11,513.59	1.49	169.51	29.91	139.60	0.21	1.10	1.67
6	137.00	966.70	0.14	1.08	9.02	0.90	7.21	8.07	1.95	26.42	6.65	46.52	8.16	18.09	2.12	12.35	1.40	60.64	1.06	11,304.11	0.55	149.96	28.24	121.72	0.23	0.41	2.24
11	19.20	1248.70	0.02	1.03	9.59	0.53	3.04	2.11	0.81	4.17	2.08	27.68	10.51	46.66	10.27	82.51	13.26	64.04	1.29	12,620.83	1.47	214.23	17.10	197.13	0.09	0.83	3.18
18	101.00	1962.10	0.05	0.34	5.67	0.28	1.71	2.11	0.46	11.75	5.21	67.15	24.87	110.83	23.31	218.03	32.08	60.18	2.19	11,046.88	1.92	503.81	10.57	493.24	0.02	0.28	4.52
23	45.50	3417.50	0.01	0.02	0.69	0.01	0.28	1.02	0.12	8.44	5.66	90.46	33.91	143.26	27.33	216.99	28.76	60.37	1.88	12,523.64	2.45	556.98	2.16	554.82	0.00	0.12	9.16
24	33.90	3659.80	0.01	0.35	2.42	0.27	1.84	1.91	0.29	11.45	7.07	94.72	26.33	77.31	10.13	65.11	6.76	60.66	1.96	12,687.47	2.61	305.98	7.09	298.89	0.02	0.19	1.93
25	81.50	421.40	0.19	0.38	5.04	0.49	3.91	4.71	1.14	14.00	4.09	28.77	5.36	12.53	1.54	9.47	1.03	63.89	0.67	11,396.00	0.49	92.44	15.67	76.77	0.20	0.43	2.86
26	44.70	4226.80	0.01	4.54	22.90	3.22	15.69	6.19	7.71	15.27	7.64	123.30	48.93	224.05	50.05	457.94	74.07	60.21	2.52	12,297.49	2.79	1061.50	60.25	1001.25	0.06	2.43	1.47
27	52.70	2809.10	0.02	8.47	62.02	4.91	25.85	10.74	5.42	17.33	6.35	84.09	31.90	141.34	29.09	256.42	36.71	58.99	2.38	12,160.40	3.50	720.64	117.41	603.23	0.19	1.21	2.36
29	96.70	220.40	0.44	0.03	3.31	0.03	0.36	0.94	0.74	5.21	1.92	23.45	8.96	45.03	9.85	98.79	16.79	64.01	1.07	11,292.50	0.83	215.41	5.41	210.00	0.03	1.03	27.52
38	45.90	3938.20	0.01	4.99	37.03	3.75	19.71	8.54	5.11	17.58	7.22	100.66	40.54	191.88	41.11	361.65	49.91	59.25	2.55	11,784.48	3.97	889.69	79.14	810.55	0.10	1.28	2.10
39	117.80	377.50	0.31	0.03	2.09	0.06	1.57	2.94	0.10	11.32	2.85	20.49	3.81	7.91	0.94	5.05	0.53	65.16	0.83	12,162.60	0.55	59.69	6.79	52.90	0.13	0.05	11.98
43	32.70	3076.50	0.01	6.70	76.65	4.72	24.27	10.41	6.83	19.60	7.62	81.98	19.04	46.40	5.18	28.50	2.88	60.21	1.51	12,578.78	1.94	340.80	129.59	211.21	0.61	1.46	3.34
44	54.70	2697.70	0.02	7.54	75.55	5.90	30.34	13.10	7.23	18.19	6.41	80.41	25.82	98.31	18.45	159.73	21.17	59.46	1.52	12,907.12	1.88	568.15	139.66	428.49	0.33	1.43	2.78
47	24.80	2720.10	0.01	4.83	70.91	2.63	12.38	5.05	3.87	11.21	4.57	64.24	21.26	76.91	14.00	105.63	13.16	58.60	1.15	11,268.17	1.87	410.67	99.68	310.99	0.32	1.57	4.87
49	35.40	3761.10	0.01	0.01	0.29	0.00	0.14	0.83	0.04	8.39	4.61	81.76	35.19	165.35	35.80	296.12	39.17	60.33	1.91	12,739.59	3.23	667.67	1.30	666.37	0.00	0.05	0.93
50	122.40	705.40	0.17	0.01	1.52	0.06	0.97	2.89	0.09	16.29	5.30	42.68	7.99	15.72	1.77	9.26	1.08	64.32	1.17	11,328.30	0.97	105.63	5.53	100.10	0.06	0.04	32.72
52	45.00	2438.60	0.02	5.52	68.98	3.32	16.33	6.41	5.48	12.21	4.54	62.12	23.58	110.97	24.38	219.00	31.69	55.65	1.83	11,486.49	2.83	594.53	106.04	488.49	0.22	1.89	3.95
55	34.40	3303.40	0.01	0.30	2.58	0.30	1.63	1.65	0.59	7.07	4.70	75.92	31.84	143.46	30.89	256.87	34.93	60.12	1.80	12,740.00	3.13	592.72	7.04	585.68	0.01	0.53	2.12

5.2.2. Lu-Hf Isotopes in Zircon

In the sample Z1220-23-2, the $\varepsilon_{\text{Hf}}(t)$ values are negative and range from -15 to -1 , with a corresponding t_{DM2} range of 2202–2453 Ma. In the case of Z1218-6, the $\varepsilon_{\text{Hf}}(t)$ ranges from -2.13 to 6.32 , with its corresponding t_{DM2} falling between 1101 and 1619 Ma. Z1230-42-4 exhibits $\varepsilon_{\text{Hf}}(t)$ values from -0.46 to -16.52 , and its corresponding t_{DM2} ranges from 1528 to 2534 Ma. For Z1230-50-1, the $\varepsilon_{\text{Hf}}(t)$ is negative (-7.46 to -11.67), and the corresponding t_{DM2} falls within the range of 1975–2211 Ma. Finally, in the case of Z1230-45-2, $\varepsilon_{\text{Hf}}(t)$ ranges from -9 to -3 , and its corresponding t_{DM2} is within the range of 1738–2092 Ma (Figure 9 and Table 5).

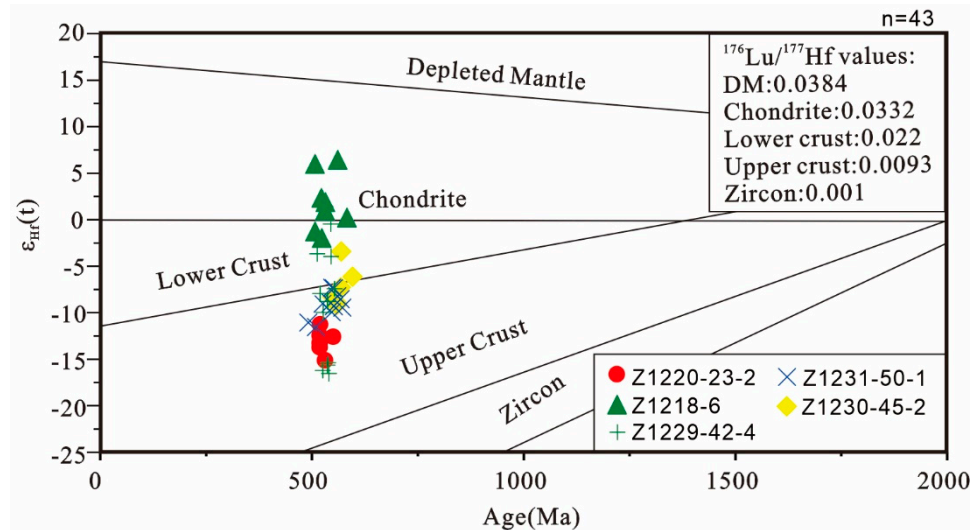


Figure 9. U-Pb age- $\varepsilon_{\text{Hf}}(t)$ variation.

Table 5. Zircon Lu-Hf isotopic data of the samples.

Sample	$^{176}\text{Yb}/^{177}\text{Hf}$	2σ	$^{176}\text{Lu}/^{177}\text{Hf}$	2σ	$^{176}\text{Hf}/^{177}\text{Hf}$	2σ	Age (Ma)	$\varepsilon_{\text{Hf}}(t)$	$T_{\text{DM1}}(\text{Ma})$	$T_{\text{DM2}}(\text{Ma})$	$f_{\text{Lu/Hf}}$
Z1220-23-2											
4	0.001318	0.000015	0.000036	0.000001	0.282071	0.000014	518	-13.4	1621	2326	-1.00
12	0.008493	0.000140	0.000304	0.000002	0.282129	0.000031	519	-11.39	1553	2202	-0.99
14	0.002127	0.000070	0.000062	0.000002	0.282011	0.000038	531	-15.27	1704	2453	-1.00
19	0.001566	0.000012	0.000045	0.000001	0.282070	0.000015	550	-12.72	1623	2309	-1.00
27	0.001262	0.000010	0.000035	0.000000	0.282094	0.000012	518	-12.58	1590	2276	-1.00
31	0.001949	0.000068	0.000056	0.000002	0.282058	0.000016	518	-13.86	1639	2355	-1.00
Z1218-6											
3	0.006438	0.000027	0.000273	0.000002	0.282511	0.000019	522	2.2	1028	1346	-0.99
9	0.011279	0.000126	0.000466	0.000005	0.282498	0.000026	528	1.77	1052	1377	-0.99
36	0.008736	0.000202	0.000374	0.000008	0.282415	0.000023	583	0.08	1164	1527	-0.99
37	0.010024	0.000094	0.000430	0.000004	0.282470	0.000032	531	0.84	1090	1438	-0.99
40	0.049057	0.000433	0.001851	0.000016	0.282433	0.000027	507	-1.42	1184	1564	-0.94
41	0.012529	0.000228	0.000534	0.000010	0.282627	0.000032	507	5.87	874	1101	-0.98
44	0.008471	0.000075	0.000339	0.000003	0.282605	0.000025	561	6.32	900	1112	-0.99
47	0.009077	0.000076	0.000397	0.000002	0.282390	0.000025	523	-2.13	1198	1619	-0.99
52	0.006321	0.000037	0.000242	0.000001	0.282493	0.000019	532	1.75	1052	1380	-0.99
Z1230-42-4											
1	0.015971	0.000678	0.000449	0.000019	0.282231	0.000018	516	-7.92	1419	1981	-0.99
3	0.003249	0.000154	0.000092	0.000005	0.281972	0.000015	537	-16.52	1757	2534	-1.00
9	0.002353	0.000029	0.000061	0.000001	0.282324	0.000022	542	-3.94	1279	1750	-1.00
27	0.005329	0.000286	0.000150	0.000009	0.281992	0.000020	522	-16.18	1734	2503	-1.00
34	0.008197	0.000586	0.000187	0.000011	0.282167	0.000038	523	-9.96	1497	2114	-0.99
39	0.002116	0.000023	0.000052	0.000001	0.282423	0.000015	541	-0.46	1143	1528	-1.00
41	0.003061	0.000069	0.000089	0.000002	0.282221	0.000020	550	-7.41	1419	1973	-1.00
46	0.005436	0.000141	0.000158	0.000004	0.282194	0.000026	533	-8.78	1459	2046	-1.00
50	0.002255	0.000041	0.000063	0.000001	0.282353	0.000026	509	-3.65	1239	1705	-1.00
52	0.015970	0.000362	0.000654	0.000013	0.282017	0.000015	535	-15.18	1722	2450	-0.98

Table 5. Cont.

Sample	$^{176}\text{Yb}/^{177}\text{Hf}$	2σ	$^{176}\text{Lu}/^{177}\text{Hf}$	2σ	$^{176}\text{Hf}/^{177}\text{Hf}$	2σ	Age (Ma)	$\varepsilon_{\text{Hf}} (\text{t})$	$T_{\text{DM1}} (\text{Ma})$	$T_{\text{DM2}} (\text{Ma})$	$f_{\text{Lu/Hf}}$
Z1219-50-1											
2	0.008867	0.000159	0.000311	0.000007	0.282166	0.000014	550	-9.43	1504	2103	-0.99
4	0.008980	0.000324	0.000289	0.000010	0.282177	0.000016	566	-8.69	1487	2066	-0.99
8	0.004610	0.000077	0.000148	0.000003	0.282152	0.000019	490	-11.18	1516	2167	-1.00
11	0.007078	0.000018	0.000211	0.000003	0.282179	0.000017	543	-9.09	1481	2074	-0.99
26	0.006352	0.000222	0.000212	0.000007	0.282219	0.000020	550	-7.52	1426	1980	-0.99
31	0.011156	0.000299	0.000383	0.000010	0.282130	0.000020	508	-11.67	1556	2211	-0.99
33	0.002440	0.000014	0.000080	0.000000	0.282189	0.000022	558	-8.37	1463	2040	-1.00
39	0.004478	0.000076	0.000148	0.000002	0.282148	0.000022	570	-9.59	1521	2125	-1.00
42	0.003002	0.000016	0.000095	0.000000	0.282149	0.000018	545	-10.07	1518	2138	-1.00
47	0.005546	0.000076	0.000174	0.000002	0.282222	0.000020	546	-7.46	1421	1975	-0.99
50	0.006224	0.000056	0.000196	0.000001	0.282185	0.000019	526	-9.25	1472	2070	-0.99
Z1230-45-2											
2	0.001276	0.000013	0.000028	0.000000	0.282194	0.000014	549	-8.35	1454	2033	-1.00
16	0.042659	0.000347	0.001306	0.000018	0.282241	0.000024	597	-6.16	1438	1930	-0.96
24	0.007720	0.000462	0.000235	0.000016	0.282214	0.000014	569	-7.31	1435	1981	-0.99
29	0.008848	0.000371	0.000335	0.000014	0.282324	0.000013	570	-3.43	1288	1738	-0.99
47	0.004942	0.000119	0.000128	0.000003	0.282169	0.000020	561	-9.01	1492	2084	-1.00
55	0.014009	0.000141	0.000432	0.000005	0.282168	0.000024	559	-9.2	1504	2092	-0.99

6. Discussion

The nature of the Prydz Pan-African tectonic belt remains a subject of debate due to research limitations on the unified East Gondwana landmass. There are conflicting opinions among researchers, with some suggesting that it is a collisional orogenic belt [11,13,16,19–21]. Others express concerns about the lack of direct indicators for specific facies, such as ophiolites, island arc accretion complexes, and high-pressure metamorphic rocks [24,26,29,34].

Based on the trace element composition of Pan-African pegmatites in the Larsemann Hills (Figure 6, Table 1), it is evident that pegmatite samples from the D₂–D₄ stage are enriched in large-ion lithophile elements (LILE) and depleted in high-field-strength elements (HFSE). The scarcity of P and Ti reflects the separation and crystallization of apatite and Ti-rich minerals. The loss of Nb and Ta may be linked to the separation and crystallization of rutile, or it could be attributed to crustal material contamination in the source area. Samples Z1220-23-2, Z1229-42-4, and Z1231-50-1 exhibit moderate negative Eu anomalies, potentially connected to separate plagioclase crystallization. In contrast, samples Z1230-45-2 and Z1218-6, being plagioclase pegmatites, show varying degrees of positive Eu anomalies.

The pegmatites in the Larsemann Hills studied in this paper are characterized as peraluminous and contain minerals such as garnet that also exhibit peraluminous characteristics. A comprehensive analysis reveals that the residual phases in the pegmatites are plagioclase and garnet. Plagioclase becomes unstable when the pressure exceeds 1.5 GPa [69]. Therefore, the formation pressure of the pegmatites is inferred to be less than 1.5 GPa, corresponding to a magmatic depth of less than 40 km [70]. The results indicate that the five samples are classified as I- and S-type granites (Figure 10a) and fractionated I-, S-, and M-type granites (Figure 10b) [71], aligning with volcanic arc granites (VAG) and syn-collisional granites (syn-COLG) (Figure 11a). They are linearly projected near the boundary between volcanic arc granite (VAG) and syn-collisional granite (syn-COLG) (Figure 11b) [72].

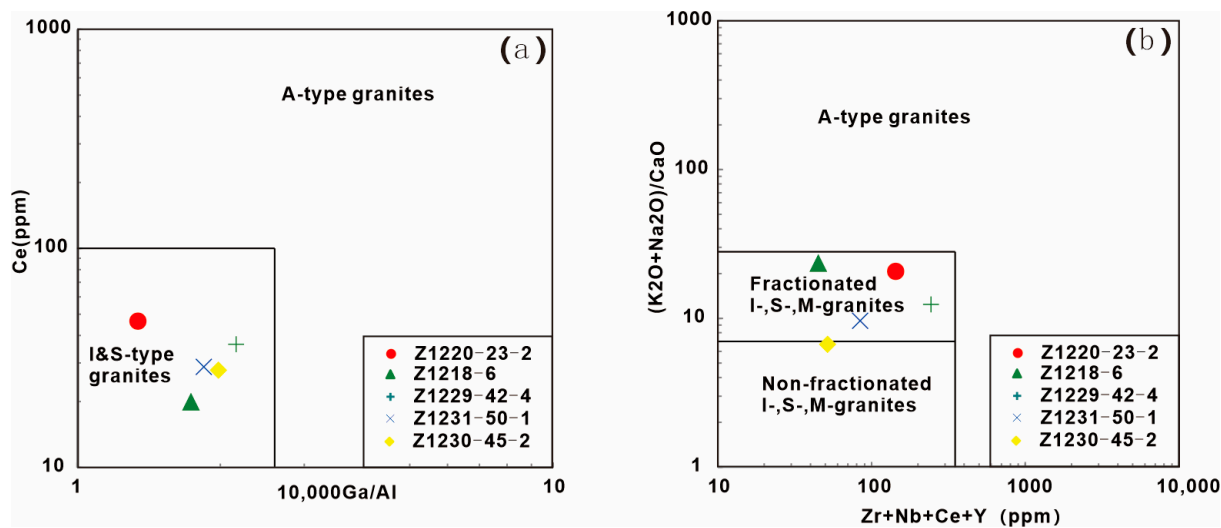


Figure 10. 10^4 Ga/Al vs. Ce (a), $\text{Zr} + \text{Nb} + \text{Ce} + \text{Y}$ vs. $(\text{K}_2\text{O} + \text{Na}_2\text{O})/\text{CaO}$ (b) classification diagrams [71] of Pan-African pegmatites in Larsemann Hills.

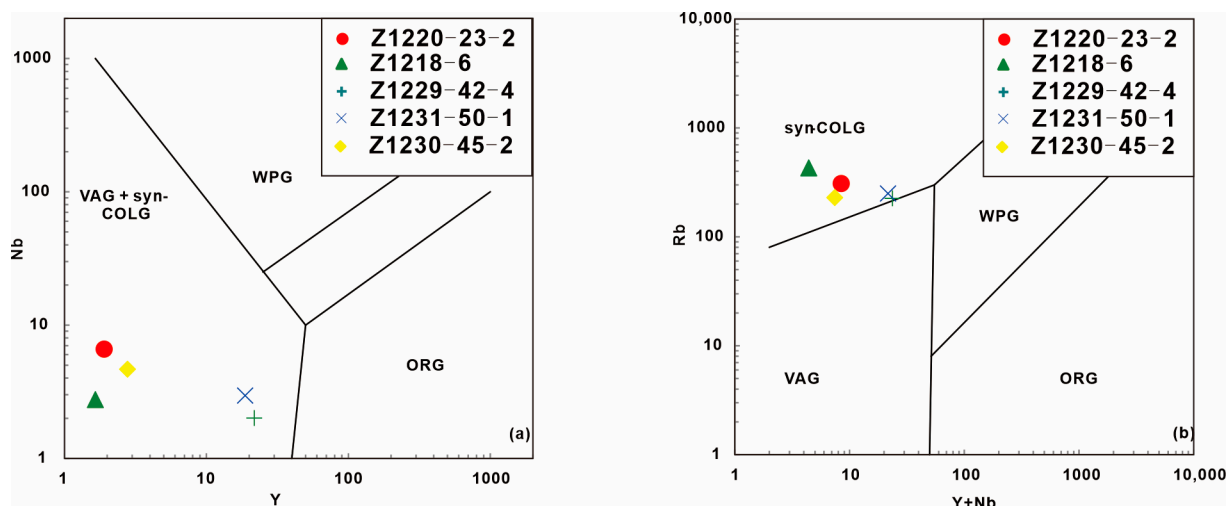


Figure 11. Discrimination diagrams of the tectonic environment of granitic pegmatites in the Larsemann Hills (a,b). Abbreviations: syn-collision granite (syn-COLG), volcanic arc granite (VAG), with plate granite (WPG), and normal and anomalous ocean ridge granite (ORG) (based on Pearce et al., 1984 [73]).

Zircon, a key mineral for U-Pb geochronology, is a stable mineral [74,75], and its Lu-Hf isotopes are extensively used in geochemical studies to understand the origin of magma and specific magmatic processes. Previous studies have shown that the genesis of magmatic rocks has two modes: (1) the partial melting of preexisting crustal material, in which the $\varepsilon_{\text{Hf}}(t)$ value of the zircons in magmatic rocks is lower than that in chondrite; (2) new crustal material or partially melted mantle material, in which the zircon $\varepsilon_{\text{Hf}}(t)$ value of magmatic rocks is higher than that of chondrite [9]. This provides conclusive evidence for identifying source areas [76]. The t_{DM2} age of zircon can offer a more precise reflection of the average retention age of the source material [77].

These features indicate a magmatic origin for the investigated zircons based on their shape, CL images, REE distribution patterns, and Th/U ratios. According to the zircon U-Pb data of the analyzed samples, it can be inferred that the Pan-African pegmatites in the Larsemann Hills formed at least 519–562 Ma, predating the emplacement of Progress granite at 514–516 Ma [12]. The chronological order of the formation of geological units, as

indicated by the zircon U-Pb ages in this study, is consistent with the field investigation results reported by [78] and Ren (personal communication). Therefore, it is unlikely that the genesis of the Larsemann Hills' Pan-African pegmatites is the result of the differentiation and crystallization of Progress granitic magma, Lines 370–372, from the petrographic descriptions and field relations; some pegmatites contain sillimanite and contact with metapelites, indicating a possible origin as a result of partial melting of the metapelites. The $^{176}\text{Lu}/^{177}\text{Hf}$ ratios of all zircons are less than 0.002, indicating that zircons have accumulated less radiogenic Hf during the evolution process after rock body formation. Thus, the zircon $^{176}\text{Lu}/^{177}\text{Hf}$ ratio can be used to elucidate genetic information during rock body formation [79]. Additionally, the $f_{\text{Lu/Hf}}$ values range from -1.00 to -0.94 , smaller than the $f_{\text{Lu/Hf}}$ values of silico-aluminous crust (-0.72) and the $f_{\text{Lu/Hf}}$ values of mafic crust (-0.34) [76]. Therefore, the t_{DM2} age more clearly reflects the time when the source material was obtained from the depleted mantle.

In the granitic pegmatite (Z1220-23-2) and the plagioclase pegmatite (Z1218-6) of the D₄ phase of the Larsemann Hills, the $\varepsilon_{\text{Hf}}(t)$ values of zircons in the granitic pegmatite (Z1220-23-2), which formed at ~ 517 Ma(D₄₋₂), range from -15.27 to -11.39 , indicating values lower than chondrite (Figure 9). The granitic pegmatite (Z1220-23-2) primarily originates from the reworked Brattstrand paragneiss [78], and its corresponding t_{DM2} is 2202 to 2453 Ma, suggesting a partial provenance relationship with the Paleoproterozoic crust. The $\varepsilon_{\text{Hf}}(t)$ values of the zircons in the plagioclase pegmatite (Z1218-6), formed at ~ 521 Ma(D₄₋₂), range from -2.13 to 6.32 . The positive $\varepsilon_{\text{Hf}}(t)$ values indicate the presence of juvenile zircons. Their corresponding t_{DM2} is 1101–1619 Ma, indicating that the plagioclase pegmatite (Z1218-6) is derived from a magma formed by the mixing of Mesoproterozoic crust-derived magma and mantle-derived magma. The $\varepsilon_{\text{Hf}}(t)$ values of zircons from the ~ 534 Ma granitic pegmatite (Z1229-42-4), formed in the D₃ stage, range from -16.52 to -0.46 . Although all $\varepsilon_{\text{Hf}}(t)$ values are negative, there is extensive variation. The corresponding t_{DM2} is 1528–2534 Ma, indicating that granitic pegmatite (Z1229-42-4) primarily results from the partial melting of Paleoproterozoic crustal material. In the granitic pegmatite (Z1230-50-1) formed at 562 ± 6 Ma (the D₂ stage) in the Larsemann Hills, the zircon $\varepsilon_{\text{Hf}}(t)$ of the granitic pegmatite (Z1230-50-1) ranges from -11.67 to -7.52 (Figure 9). The corresponding t_{DM2} is 1975–2211 Ma, suggesting that the granitic pegmatite (Z1220-50-1) primarily results from the partial melting of Paleoproterozoic crustal material. In the plagioclase pegmatite (Z1230-45-2), formed at 546 ± 6 Ma(D₂), the $\varepsilon_{\text{Hf}}(t)$ value of the zircons in the plagioclase pegmatite (Z1230-45-2) ranges from -9.20 to -3.43 , indicating a lower value than that of chondrite in both the zircon U-Pb age and $\varepsilon_{\text{Hf}}(t)$ diagrams. The corresponding t_{DM2} is 1738–2084 Ma, suggesting that the plagioclase pegmatite (Z1230-45-2) primarily originates from the partial melting of Paleoproterozoic ancient crustal material. It is inferred that the D₂–D₄ pegmatites have multiple different source areas, with D₂–D₃ pegmatites mainly derived from Paleoproterozoic crustal material. The D₄-stage pegmatite exhibits characteristics of both Paleo–Mesoproterozoic crustal material sources and mantle material sources. The D₄₋₁ pegmatite (~ 521 Ma) suggests both Paleo–Mesoproterozoic crustal and mantle origin. This aligns with the formation age and structural attributes of the Pan-African post-collisional granite in Prydz Bay [12]. The D₄₋₂ pegmatite (~ 517 Ma) originates from the crust layers.

Combining rock geochemical and zircon characteristics, the Pan-African pegmatites in the Larsemann Hills likely originated from the Pan-African high-grade tectonic mobile belt of the Gondwana paleocontinent (Figure 12a), forming the D_{2–4} stage pegmatites (562–517 Ma). This was followed by lithospheric thinning (Figure 12b). These results provide new insights into the origin of pegmatites in the D₂–D₄ stage and effectively confirm the presence of a critical Gondwana paleocontinental extension zone near Prydz Bay.

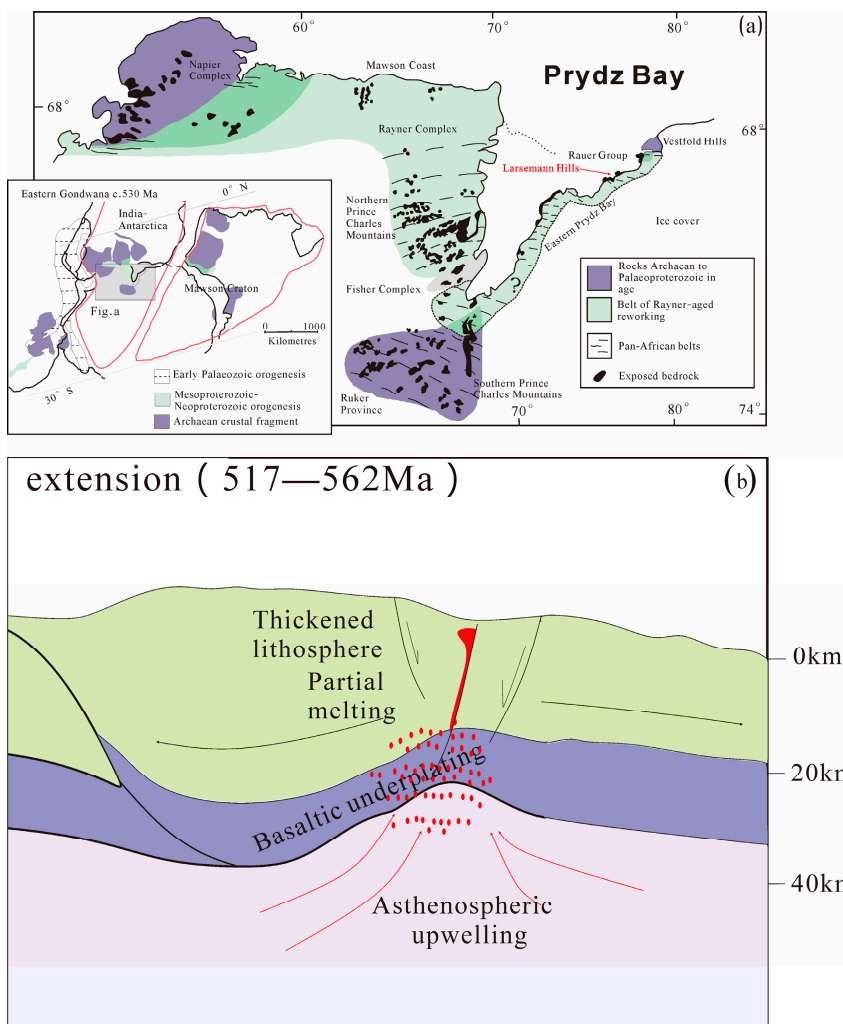


Figure 12. Simplified geological map of Prydz Bay in East Antarctica (a) (modified after Ren et al. [40]). Simplified evolution of Pan-African pegmatites in Prydz Bay (b).

7. Conclusions

Based on petrography, U-Pb geochronology, Lu-Hf isotopes, and major and trace element data on the pegmatites from the Larsemann Hills, the following conclusions were obtained:

1. According to geological and geochronological data, the pegmatites in the Larsemann Hills formed during the Pan-African D₂-D₄ stage. The D₂ pegmatite formed between 546 and 562 Ma, the D₃ pegmatite around 534 Ma, and the D₄ pegmatite between 517 and 521 Ma. These pegmatites were formed during the Pan-African tectono-thermal event in an environment marked by an extension. It is plausible that a prominent breakup zone may be situated near the Larsemann Hills.
2. The Pan-African-period pegmatites discovered in the Larsemann Hills have different sources of material. Pegmatites from the D₂-D₃ period are considered to primarily originate from Paleoproterozoic crustal materials. In contrast, pegmatites from the D₄₋₁ stage (~521 Ma) have sources from both Paleo-Mesoproterozoic crustal material sources and mantle material sources. Pegmatites from the D₄₋₂ stage (~517 Ma) have sources that originated from the crust layers.

Author Contributions: Conceptualization, S.Z. and Y.C.; methodology, S.Z.; software, S.Z.; validation, Y.C. and L.R.; formal analysis, S.Z.; investigation, S.Z., H.Z., S.C. and W.W.; resources, Y.C.; data curation, S.Z.; writing—original draft preparation, S.Z.; writing—review and editing, Y.C., L.R.

and S.L.; visualization, S.Z.; supervision, Y.C.; project administration, Y.C.; funding acquisition, Y.C. All authors have read and agreed to the published version of the manuscript.

Funding: This research was funded by the National Key Research and Development Program of China (2022YFC2807405) and the Natural Science Foundation of China (Grant nos. 41530209, 41876227, 91958216).

Data Availability Statement: Data is contained within the article.

Conflicts of Interest: The authors declare no conflict of interest.

References

- Carson, C.J.; Dirks, P.H.G.M.; Hand, M.; Sims, J.P.; Wilson, C.J.L. Compressional and extensional tectonics in low-medium pressure granulites from the Larsemann Hills, East Antarctica. *Geol. Mag.* **1995**, *132*, 151–170. [[CrossRef](#)]
- Dirks, P.; Carson, C.; Wilson, C. The deformational history of the Larsemann Hills, Prydz Bay: The importance of the Pan-African (500 Ma) in East Antarctica. *Antarct. Sci.* **1993**, *5*, 179–192. [[CrossRef](#)]
- Grew, E.S.; Carson, C.J.; Christy, A.G.; Boger, S.D. Boron- and phosphate-rich rocks in the Larsemann Hills, Prydz Bay, East Antarctica: Tectonic Implications. *Geol. Soc. Lond. Spec. Publ.* **2013**, *383*, 73–94. [[CrossRef](#)]
- Liu, X.H.; Tong, L.X.; Li, J.L.; Zhao, Y.; Ren, L.D.; Wang, Y.B. Tectonic evolution of East Antarctica shield during Mesoproterozoic and Early Palaeozoic. In *Program and Extended Abstracts, Conference on Geology across Taiwan Strait*; China Geological Association Press: Taipei, Taiwan, 1995; Volume 2, pp. 165–169. (In Chinese)
- Ren, L.; Zhao, Y.; Liu, X.; Chen, T. Re-examination of the metamorphic evolution of the Larsemann Hills, East Antarctica. In *Recent Progress in Antarctic Earth Science*; Yoshida, Y., Kaminuma, K., Shiraishi, K., Eds.; Terrapub: Tokyo, Japan, 1992; pp. 145–153.
- Tong, L.; Liu, Z.; Li, Z.-X.; Liu, X.; Zhou, X. Poly-phase metamorphism of garnet-bearing mafic granulite from the Larsemann Hills, East Antarctica: P-T path, U-Pb ages and tectonic implications. *Precambrian Res.* **2019**, *326*, 385–398. [[CrossRef](#)]
- Wang, W.R.Z.; Zhao, Y.; Wei, C.J.; Daczko, N.R.; Liu, X.C.; Xiao, W.J.; Zhang, Z.Y. High-Ultrahigh Temperature Metamorphism in the Larsemann Hills: Insights into the Tectono-thermal Evolution of the Prydz Bay Region, East Antarctica. *J. Petrol.* **2022**, *63*, egac002. [[CrossRef](#)]
- Zhao, Y.; Song, B.; Wang, Y.; Ren, L.; Li, J.; Chen, T. Geochronology of the late granite in the Larsemann Hills, East Antarctica. In *Recent Progress in Antarctic Earth Science*; Yoshida, Y., Kaminuma, K., Shiraishi, K., Eds.; Terra Scientific Publishing: Tokyo, Japan, 1992; pp. 155–161.
- Zong, S.; Ren, L.; Wu, M. Grenville-age metamorphism in the Larsemann Hills: P-T evolution of the felsic orthogneiss in the Brønnes Peninsula, East Antarctica. *Int. Geol. Rev.* **2020**, *63*, 866–881. [[CrossRef](#)]
- Boger, S.D. Antarctica—Before and after Gondwana. *Gondwana Res.* **2011**, *19*, 335–371. [[CrossRef](#)]
- Boger, S.D.; Wilson, C.; Fanning, C.M. Early Paleozoic tectonism within the East Antarctic craton, The final suture between east and west Gondwana? *Geology* **2001**, *29*, 463–466. [[CrossRef](#)]
- Carson, C.J.; Fanning, C.M.; Wilson, C.J.L. Timing of the progress granite, Larsemann hills, Additional evidence for early Palaeozoic orogenesis within the east Antarctic Shield and implications for Gondwana assembly. *Aust. J. Earth Sci.* **1996**, *43*, 539–553. [[CrossRef](#)]
- Fitzsimons, I.C.W. Grenville-age basement provinces in East Antarctica: Evidence for three separate collisional. *Geology* **2000**, *28*, 879–882. [[CrossRef](#)]
- Fitzsimons, I.C.W. Metapelitic migmatites from Brattstrand bluffs, east Antarctica—Metamorphism, melting, and exhumation of the mid crust. *J. Petrol.* **1996**, *37*, 395–414. [[CrossRef](#)]
- Harley, S.L. Archaean-cambrian crustal development of East Antarctica: Metamorphic characteristics and tectonic implications. In *Proterozoic East Gondwana: Supercontinent Assembly and Breakup*; Yoshida, M., Windley, B.F., Dasgupta, S., Eds.; Geological Society, London, Special Publications: London, UK, 2003; Volume 206, pp. 203–230.
- Hensen, B.J.; Zhou, B. East Gondwana amalgamation by Pan-African collision? Evidence from Prydz Bay, east Antarctica. In *The Antarctic Region: Geological Evolution and Processes*; Ricci, C.A., Ed.; Terra Antarctica Publishing: Siena, Italy, 1997; pp. 115–119.
- Hu, J.; Liu, X.; Zhao, Y.; Xu, G.; Ren, L. Advances in the Study of the Orogeny and Structural Deformation of Prydz Tectonic Belt in East Antarctica. *Acta Geosci. Sinica* **2008**, *29*, 343–354. (In Chinese with English Abstract)
- Liu, X.C.; Zhao, Y.; Liu, X.; Hu, J.M.; Xu, G. Evolution of high-grade metamorphism in the Prydz Belt, East Antarctica. *Earth Sci. Front.* **2007**, *14*, 056–063. (In Chinese with English Abstract)
- Liu, X.C.; Zhao, Y.; Song, B.; Liu, J.; Cui, J. SHRIMP U–Pb zircon geochronology of high-grade rocks and charnockites from the eastern Amery Ice Shelf and southwestern Prydz Bay, East Antarctica: Constraints on Late Mesoproterozoic to Cambrian tectonothermal events related to supercontinent assembly. *Gondwana Res.* **2009**, *16*, 342–361. [[CrossRef](#)]
- Liu, X.H.; Zhao, Y.; Tong, L.X.; Ren, L.D. The East Antarctic Block in the Tectonic Evolution of the Rodinia-Gondwana Super Continents. *Chin. J. Polar Res.* **2002**, *24*, 35–40. (In Chinese with English Abstract)
- Zhao, Y.; Liu, X.H.; Liu, X.C.; Song, B. *Pan-African Events in Prydz Bay, East Antarctica, and Their Implications for East Gondwana tectonics*; Geological Society, London, Special Publications: London, UK, 2003; Volume 206, pp. 231–245.

22. Dirks, P.H.G.M.; Hand, M. Clarifying temperature-pressure paths via structures in granulite from the Bolingen Islands, Antarctica. *J. Geol. Soc. Aust.* **1995**, *42*, 157–172. [[CrossRef](#)]
23. Dirks, P.H.G.M.; Wilson, C.J.L. Crustal evolution of the East Antarctic mobile belt in Prydz Bay: Continental collision at 500 Ma? *Precambrian Res.* **1995**, *75*, 189–207. [[CrossRef](#)]
24. Grew, E.S.; Edward, S.; Carson, C.J.; Christy, A.G.; Maas, R.; Yaxley, G.M.; Boger, S.D.; Fanning, C.M. New constraints from U-Pb, Lu-Hf, and Sm-Nd isotopic data on the timing of sedimentation and felsic magmatism in the Larsemann Hills, Prydz Bay, East Antarctica. *Precambrian Res.* **2012**, *206*, 87–108. [[CrossRef](#)]
25. Kelsey, D.; Hand, M.; Clark, C.; Wilson, C. On the application of in situ monazite chemical geochronology to constraining P-T-t histories in high-temperature ($>850^{\circ}\text{C}$) polymetamorphic granulites from Prydz Bay, East Antarctica. *J. Geol. Soc.* **2007**, *164*, 667–683. [[CrossRef](#)]
26. Phillips, G.; Wilson, C.J.L.; Phillips, D.; Szczepanski, S.K. Thermochronological ($^{40}\text{Ar}/^{39}\text{Ar}$) evidence of Early Palaeozoic basin inversion within the southern Prince Charles Mountains, East Antarctica: Implications for East Gondwana. *J. Geol. Soc.* **2007**, *164*, 771–784. [[CrossRef](#)]
27. Ren, L.; Li, C.; Wang, Y.; Liu, P. On Constraining the Pan-African High-grade Metamorphism Time Of The Larsemann Hills, East Antarctica. *Chin. J. Polar Res.* **2016**, *28*, 451–461, (In Chinese with English Abstract).
28. Tong, L.; Jahn, B.-M.; Liu, X.; Liang, X.; Xu, Y.-G.; Ionov, D. Ultramafic to mafic granulites from the Larsemann Hills, East Antarctica: Geochemistry and tectonic implications. *J. Asian Earth Sci.* **2017**, *145*, 679–690. [[CrossRef](#)]
29. Tong, L.; Liu, X.; Wang, Y.; Liang, X. Metamorphic P-T paths of metapelitic granulites from the Larsemann Hills, East Antarctica. *Lithos* **2014**, *192–195*, 102–115. [[CrossRef](#)]
30. Tong, L.; Wilson, C.J.L. Tectonothermal evolution of the ultrahigh temperature metapelites in the Rauer Group, east Antarctica. *Precambrian Res.* **2006**, *149*, 1–20. [[CrossRef](#)]
31. Tong, L.; Wilson, C.; Liu, X. A high-grade event of ~ 1100 Ma preserved within the ~ 500 Ma mobile belt of the Larsemann Hills, east Antarctica: Further evidence from $^{40}\text{Ar}-^{39}\text{Ar}$ dating. *Terra Antarct.* **2002**, *9*, 73–86.
32. Tong, L.; Liu, X.; Zhang, L.; Chen, H.; Chen, F. The Ar-Ar ages of hornblendes in Grt-Pl-bearing amphibolite from the Larsemann Hills, East Antarctica, and their geological implication. *Adv. Polar Sci.* **1998**, *9*, 79–91.
33. Wang, Y.; Liu, D.; Chung, S.; Tong, L.; Ren, L. SHRIMP zircon age constraints from the Larsemann Hills region, Prydz Bay, for a Late Mesoproterozoic to Early Neoproterozoic tectono-thermal event in East Antarctica. *Am. J. Sci.* **2008**, *308*, 573–617. [[CrossRef](#)]
34. Wilson, C.J.L.; Quinn, C.; Tong, L.; Phillips, D. Early Palaeozoic intracratonic shears and post-tectonic cooling in the Rauer Group, Prydz Bay, East Antarctica constrained by Ar/Ar thermochronology. *Antarct. Sci.* **2007**, *19*, 339–353. [[CrossRef](#)]
35. Li, M. Geochronology and Geochemistry of Granitoids from the Prydz Belt, East Antarctica, and Their Tectonic Implications. Ph.D. Thesis, Chinese Academy of Geological Sciences, Beijing, China, 2006.
36. Stüwe, K.; Braun, H.; Peer, H. Geology and structure of the Larsemann Hills area, Prydz Bay, East Antarctica. *Aust. J. Earth Sci.* **1989**, *36*, 219–241. [[CrossRef](#)]
37. Jahns, R.; Burnham, C. Experimental studies of pegmatite genesis: I. A model for the derivation and crystallization of granitic pegmatites. *Econ. Geol.* **1969**, *64*, 843–864. [[CrossRef](#)]
38. London, D. Granitic pegmatites: An assessment of current concepts and directions for the future. *Lithos* **2005**, *80*, 281–303. [[CrossRef](#)]
39. Ren, L. Discussion on the origin of sillimanite. *Acta Petrol. Mineral.* **2022**, *41*, 437–445, (In Chinese with English Abstract).
40. Ren, L.; Zong, S.; Wang, Y.; Li, C. Distribution domains of the Pan-African event in East Antarctica and adjacent areas. *Adv. Polar Sci.* **2018**, *29*, 87–107.
41. Spreitzer, S.K.; Walters, J.B.; Cruz-Uribe, A.; Williams, M.L.; Yates, M.G.; Jercinovic, M.J.; Grew, E.S.; Carson, C.J. Monazite petrochronology of polymetamorphic granulite-facies rocks of the Larsemann Hills, Prydz Bay, East Antarctica. *J. Metamorph. Geol.* **2021**, *39*, 1205–1228. [[CrossRef](#)]
42. Spreitzer, S.K. In Situ Dating of Multiple Events in Granulite-Facies Rocks of the Larsemann Hills, Prydz Bay, East Antarctica Using Electron Microprobe Analysis of Monazite. Master’s Thesis, University of Maine, Orono, ME, USA, 2017.
43. Liu, F.; Robinson, P.T.; Gerdes, A.; Xue, H.; Liu, P.; Liou, J.G. Zircon U-Pb ages, REE concentrations and Hf isotope compositions of granitic leucosome and pegmatite from the north Sulu UHP terrane in China: Constraints on the timing and nature of partial melting. *Lithos* **2010**, *117*, 247–268. [[CrossRef](#)]
44. Black, L.; Harley, S.; Sun, S.; McCulloch, M. The Rayner Complex of East Antarctica: Complex isotopic systematics within a Proterozoic mobile belt. *J. Metamorph. Geol.* **1987**, *5*, 1–26. [[CrossRef](#)]
45. Sheraton, J.W.; Black, L.P.; McCulloch, M.T. Regional geochemical and isotopic characteristics of high-grade metamorphics of the Prydz Bay area: The extent of proterozoic reworking of Qrchaean continental crust in East Antarctica. *Precambrian Res.* **1984**, *26*, 169–198. [[CrossRef](#)]
46. Wang, Y.; Zhao, Y.; Ren, L.; Chen, T.; Liu, X.; Tong, L. Geochemical characteristics and medium pressure granulite facies metamorphism of mafic granulite rocks from the Larsemann Hills, East Antarctica. *Antarct. Res.* **1994**, *6*, 4–14. (In Chinese with English Abstract)
47. Yu, L.J.; Liu, X.H.; Zhao, Y.; Ju, Y.T.; Liu, X.C. Metamorphism of mafic granulites in the Grove Mountains, East Antarctica. *Acta Petrol. Sin.* **2002**, *18*, 501–506. (In Chinese with English Abstract)

48. Zong, S.; Ren, L.; Wu, M.; Xu, H.; Zhu, S. Whole-Rock Geochemistry, Zircon U-Pb geochronology, and Lu-Hf isotopic constraints on metasedimentary rocks (*Paragneisses*) in Stornes Peninsula, Larsemann Hills, East Antarctica. *Int. Geol. Rev.* **2023**, *65*, 317–333. [[CrossRef](#)]
49. MacGregor, J.; Grew, E.S.; De Hoog, J.C.M.; Harley, S.L.; Kowalski, P.M.; Yates, M.G.; Carson, C.J. Boron isotopic composition of tourmaline, prismatic, and grandidierite from granulite facies paragneisses in the Larsemann Hills, Prydz Bay, East Antarctica: Evidence for a non-marine evaporite source. *Geochim. Cosmochim. Acta* **2013**, *123*, 261–283. [[CrossRef](#)]
50. Ren, L.; Liu, X.H. Occurrence of the assemblage grandidierite, kornerupine, and tourmaline in Antarctica. *Antarct. Res.* **1993**, *6*, 1205–1208. (In Chinese with English Abstract)
51. Fitzsimons, I. The Brattstrand Paragneiss and the Søstrene Orthogneiss: A review of Pan-African metamorphism and Grenvillian relics in southern Prydz Bay. In *The Antarctic Region; Geological Evolution and Processes*; International Symposium on Antarctic Earth Sciences; Terra Antarctica: Siena, Italy, 1997; pp. 121–130.
52. Carson, C.J.; Powell, R.; Wilson, C.J.L.; Dirks, P.H.G.M. Partial melting during tectonic exhumation of a granulite terrane: An example from the Larsemann Hills, East Antarctica. *J. Metamorph. Geol.* **2010**, *28*, 105–126. [[CrossRef](#)]
53. Li, M.; Liu, X.; Zhao, Y. Zircon U-Pb ages and geochemistry of granitoids from Prydz Bay, East Antarctica, and their tectonic significance. *Acta Geol. Sin.* **2007**, *23*, 1055–1066. (In Chinese with English Abstract)
54. Hu, J.; Wang, W.; Zhao, Y.; Liu, X.C.; Chen, H.; Dong, X. Sequence and tectonic deformation process of the metamorphic complex in the Larsemann Hills, East Antarctica. *J. Geomech.* **2021**, *27*, 719–735. (In Chinese with English Abstract)
55. Wang, Y. Studies on the Geochronology, Geochemistry of the High-Grade Gneiss of the Larsemann Hills and its Adjacent Region, East Antarctica. Ph.D. Thesis, Chinese Academy of Geological Sciences, Beijing, China, 2002.
56. Jin, X.; Zhu, H. Determination of 43 Trace Elements in Rock Samples by Double Focusing High-Resolution Inductively Coupled Plasma-Mass Spectrometry. *Chin. J. Anal. Chem.* **2000**, *5*, 563–567. (In Chinese)
57. Liu, Y.; Zhao, C.; Zong, K.; Gao, C.; Gao, S.; Xu, J.; Chen, H. Reappraisal and refinement of zircon U-Pb isotope and trace element analyses by LA-ICP-MS. *Chin. Sci. Bull.* **2010**, *51*, 537–571. [[CrossRef](#)]
58. Ludwig, K.R. *ISOPLOT 3.0: Special Publication 4.70. Computer Program*; BerkeleyGeochronology Center: Berkeley, CA, USA, 2003.
59. Peccerillo, A.; Taylor, S.R. Geochemistry of eocene calc-alkaline volcanic rocks from the Kastamonu area. *North. Turk. Contrib. Mineral. Petrol.* **1976**, *58*, 63–81. [[CrossRef](#)]
60. Middlemost, E.A.K. *Magmas and Magmatic Rocks: An Introduction to Igneous Petrology*; Longman: Harlow Essex, UK, 1985.
61. Maniar, P.D.; Piccoli, P.M. Tectonic discrimination of granitoids. *Geol. Soc. Am. Bull.* **1989**, *101*, 635–643. [[CrossRef](#)]
62. Chen, Y.; Niu, Y.; Xue, Q.; Gao, Y.; Castillo, P. An iron isotope perspective on back-arc basin development: Messages from Mariana Trough basalts. *Earth Planet. Sci. Lett.* **2021**, *572*, 117–133. [[CrossRef](#)]
63. Sun, S.-S.; McDonough, W.F. Chemical and isotopic systematics of oceanic basalts: Implications for mantle composition and processes. *Geol. Soc. Lond. Spec. Publ.* **1989**, *42*, 313–345. [[CrossRef](#)]
64. McDonough, W.F.; Sun, S.-S. The composition of the Earth. *Chem. Geol.* **1995**, *120*, 223–253. [[CrossRef](#)]
65. Hoskin, P.W.O.; Schaltegger, U. The composition of zircon and igneous and metamorphic petrogenesis. *Rev. Mineral. Geochem.* **2003**, *53*, 25–104. [[CrossRef](#)]
66. Block, S. Paleoproterozoic juvenile crust formation and stabilization in the south-eastern West African Craton (Ghana); New insights from U-Pb-Hf zircon data and geochemistry. *Precambrian Res.* **2016**, *287*, 1–30. [[CrossRef](#)]
67. Corfu, F.; Hanchar, J.M.; Hoskin, P.W.O.; Kinny, P. Atlas of Zircon Textures. *Rev. Mineral. Geochem.* **2003**, *53*, 469–500. [[CrossRef](#)]
68. Hoskin, P.W.O. Trace element composition of hydrothermal zircon and the alteration of hadean zircon from the Jack Hill, Australia. *Geochim. Et Cosmochimica Acta* **2005**, *69*, 637–648. [[CrossRef](#)]
69. Sen, C.; Dunn, T. Dehydration melting of a basaltic composition amphibolite at 1.5 and 2.0 GPa: Implications for the origin of adakites. *Contrib. Mineral. Petrol.* **1994**, *117*, 394–409. [[CrossRef](#)]
70. Wu, Q.; Niu, M.; Zhu, G.; Wang, T.; Fei, L. Zircon U-Pb age, petrogenesis of the Changgang A-type granites in the Lujiang segment of the Tan-Lu fault zone and their implication. *Acta Petrol. Sin.* **2016**, *32*, 1031–1048. (In Chinese with English Abstract).
71. Whalen, J.B.; Currie, K.L.; Chappell, B.W. A-type granites: Geochemical characteristics, discrimination and petrogenesis. *Contrib. Mineral. Petrol.* **1987**, *95*, 407–419. [[CrossRef](#)]
72. Chen, S.C.; Yu, J.J.; Bi, M.F. Extraction of fractionated interstitial melt from a crystal mush system generating the Late Jurassic high-silica granites from the Qitianling composite pluton, South China: Implications for greisen-type tin mineralization. *Lithos Int. J. Mineral. Petrol. Geochem.* **2021**, *382–383*, 105952. [[CrossRef](#)]
73. Pearce, J.A.; Harris, N.B.; Tindle, A.G. Trace Element Discrimination Diagrams for the Tectonic Interpretation of Granitic Rocks. *J. Petrol.* **1984**, *25*, 956–983. [[CrossRef](#)]
74. Fedo, C.M.; Sircombe, K.N.; Rainbird, R.H. Detrital zircon analysis of the sedimentary record. *Rev. Mineral. Geochem.* **2003**, *53*, 277–303. [[CrossRef](#)]
75. Gehrels, G. Detrital zircon U-Pb geochronology applied to tectonics. *Annu. Rev. Earth Planet. Sci.* **2014**, *42*, 127–149. [[CrossRef](#)]
76. Wu, F.; Li, X.; Zheng, Y.; Gao, S. Lu-Hf isotopic systematics and their applications in petrology. *Acta Petrol. Sin.* **2007**, *23*, 185–220. (In Chinese with English Abstract)
77. Wu, F.; Li, X.; Yang, J.; Zheng, Y. Discussions on the petrogenesis of granites. *Acta Geol. Sin.* **2007**, *23*, 1217–1238. (In Chinese with English Abstract)

78. Maas, R.; Grew, E.S.; Carson, C.J. Isotopic constraints (Pb, Rb-Sr, Sm-Nd) on the sources of early Cambrian pegmatites with boron and beryllium minerals in the Larsemann Hills, Prydz Bay, Antarctica. *Can. Mineral.* **2015**, *53*, 249–272. [[CrossRef](#)]
79. Amelin, Y.; Lee, D.-C.; Halliday, A. Early-middle Archaean crustal evolution deduced from Lu-Hf and U-Pb isotopic studies of single zircon grains. *Geochim. Cosmochim. Acta* **2000**, *64*, 4205–4225. [[CrossRef](#)]

Disclaimer/Publisher’s Note: The statements, opinions and data contained in all publications are solely those of the individual author(s) and contributor(s) and not of MDPI and/or the editor(s). MDPI and/or the editor(s) disclaim responsibility for any injury to people or property resulting from any ideas, methods, instructions or products referred to in the content.